Henri Gonçalves Mendonça

Superconductivity in Chromium-pnictides: a Matrix Random Phase Approximation analysis

Uberlândia, Minas Gerais, Brazil

2024

Henri Gonçalves Mendonça

Superconductivity in Chromium-pnictides: a Matrix Random Phase Approximation analysis

Master Thesis presented to the Graduate Program in Physics at the Federal University of Uberlândia as a partial requirement to obtain the degree of Master in Physics.

Federal University of Uberlândia – UFU

Physics Institute – INFIS

Supervisor: Prof. Dr. George Balster Martins

Uberlândia, Minas Gerais, Brazil

2024

Dados Internacionais de Catalogação na Publicação (CIP)
Sistema de Bibliotecas da UFU, MG, Brasil.

M539s 2024

Mendonça, Henri Gonçalves, 1999-
Superconductivity in Chromium-pnictides [recurso eletrônico] : a matrix random phase approximation analysis / Henri Gonçalves Mendonça. - 2024.

Orientador: George Balster Martins.
Dissertação (Mestrado) - Universidade Federal de Uberlândia, Programa de Pós-graduação em Física.
Modo de acesso: Internet.
Disponível em: http://doi.org/10.14393/ufu.di.2024.5113
Inclui bibliografia.
Inclui ilustrações.

1. Física. I. Martins, George Balster, 1962-, (Orient.). II. Universidade Federal de Uberlândia. Programa de Pós-graduação em Física. III. Título.

CDU: 53

André Carlos Francisco
Bibliotecário Documentalista - CRB-6/3408

UNIVERSIDADE FEDERAL DE UBERLÂNDIA
Coordenação do Programa de Pós-Graduação em Física
Av. João Naves de Ávila, 2121, Bloco 1A, Sala 213 - Bairro Santa Mônica, Uberlândia-MG, CEP 38400-902
Telefone: (34) 3239-4309 - www.infis.ufu.br - cpgfisica@ufu.br

ATA DE DEFESA - PÓS-GRADUAÇÃO

Programa de Pós-Graduação em:	Física				
Defesa de:	Dissertação de Mestrado				
Data:	01 de agosto de 2024	Hora de início:	14:00	Hora de encerramento:	16:05
Matrícula do Discente:	12222FIS003				
Nome do Discente:	Henri Gonçalves Mendonça				
Título do Trabalho:	Superconductivity in Chromium-pnictides: a Random Phase Approximation analysis				
Área de concentração:	Física				
Linha de pesquisa:	Sistemas nanoestruturados				
Projeto de Pesquisa de vinculação:	N.A				

Reuniu-se por meio de videoconferencia, a Banca Examinadora, designada pelo Colegiado do Programa de Pós-graduação em Física da Universidade Federal de Uberlândia - UFU, assim composta: Professores Doutores: Edson Vernek - INFIS/UFU, Luis Gregorio Dias da Silva - USP/SP e George Balster Martins - INFIS/UFU, presidente da banca.

Iniciando os trabalhos o presidente da mesa, Prof. George Balster Martins apresentou a Comissão Examinadora e o candidato, agradeceu a presença do público, e concedeu ao discente a palavra para a exposição do seu trabalho. A duração da apresentação do Discente e o tempo de arguição e resposta foram conforme as normas do Programa.

A seguir o senhor(a) presidente concedeu a palavra, pela ordem sucessivamente, aos(às) examinadores(as), que passaram a arguir o(a) candidato(a). Ultimada a arguição, que se desenvolveu dentro dos termos regimentais, a Banca, em sessão secreta, atribuiu o resultado final, considerando o(a) candidato(a):

Aprovado

Esta defesa faz parte dos requisitos necessários à obtenção do título de Mestre.

O competente diploma será expedido após cumprimento dos demais requisitos, conforme as normas do Programa, a legislação pertinente e a regulamentação interna da UFU.

Nada mais havendo a tratar foram encerrados os trabalhos. Foi lavrada a presente ata que após lida e achada conforme foi assinada pela Banca Examinadora.

Documento assinado eletronicamente por **Edson Vernek**, **Presidente**, em 02/08/2024, às 09:17, conforme horário oficial de Brasília, com fundamento no art. 6º, § 1º, do Decreto nº 8.539, de 8 de outubro de 2015.

Documento assinado eletronicamente por **George Balster Martins**, **Professor(a) do Magistério Superior**, em 02/08/2024, às 09:21, conforme horário oficial de Brasília, com fundamento no art. 6º, § 1º, do Decreto nº 8.539, de 8 de outubro de 2015.

Documento assinado eletronicamente por **Luis Gregório Godoy de Vasconcellos Dias da Silva**, **Usuário Externo**, em 02/08/2024, às 15:54, conforme horário oficial de Brasília, com fundamento no art. 6º, § 1º, do Decreto nº 8.539, de 8 de outubro de 2015.

A autenticidade deste documento pode ser conferida no site https://www.sei.ufu.br/sei/controlador_externo.php?acao=documento_conferir&id_orgao_acesso_externo=0, informando o código verificador **5573673** e o código CRC **BDDA4B04**.

Referência: Processo nº 23117.048821/2024-09 SEI nº 5573673

Acknowledgements

Primeiramente, dedico essa dissertação à minha família Vanêssa Santos Mendonça e Eduardo Gonçalves Mendonça, que sempre me apoiaram durante todo o Mestrado.

Também gostaria de agradecer e dedicar essa dissertação à minha companheira de vida Gabriela Aparecida Santos, que está ao meu lado me incentivando e me apoiando sempre.

Não poderia esquecer também na querida Amora, uma pequena companheira que fica ao meu lado a todo momento, e sua maneira tornou minha vida mais feliz.

Também aos amigos Melissa Naomi, Alessandra Köth, Rafael Cambraia e Daniela Santos pelos conselhos e apoio.

Em especial, dedico esse trabalho ao meu orientador e amigo prof. Dr. George Balster Martins, que tanto me ajudou e me aconselhou durante minha graduação e meu mestrado, no âmbito profissional e pessoal.

Por último agradeço ao meu pai Adenicio Gonçalves Mendonça Junior, que foi e continuará sendo meu exemplo de vida.

"A sabedoria não vem do acerto,
mas do aprendizado com os erros."
(Monja Coen)

Abstract

Unconventional superconductivity has been an important topic of research since its discovery in $CeCu_2Si_2$ (with $T_c = 0.7K$), by Frank Steglich and collaborators in 1979. Its importance greatly increased in 1986 when Bednorz and Müller discovered superconductivity with $T_c = 35K$ in a cuprate ceramic material. Since then, several different families of unconventional superconductors have been discovered. In all of them, the pairing mechanism is believed to not be via phonons, thus the 'unconventional' sobriquet. All of these families clearly present electronic correlations, which are universally believed to be involved in the pairing mechanism. The fact that the many-body problem involved has no known solution explains the longevity of this problem. In this dissertation, we apply the Matrix Random Phase Approximation to study superconductivity in LaCrAsO. We vary the chemical potential to induce a Lifshitz transition, i.e., a change in the topology of the Fermi surface, and study superconductivity across this transition. We find that spin singlet pairing is induced by spin fluctuations of ferromagnetic character, which results in the triplet pairing being competitive with the singlet pairing, although not dominant. In addition, the d_{xy} (B_{2g}) symmetry of the gap function (with nodes along the coordinate axes)does not vary across the Lifshitz transition. Finally, across the Lifshitz transition, the outer edges of the electron pockets, close to the Brillouin zone boundary, accumulate the majority of the amplitude of the gap function, while the hole pocket (located around the Brillouin zone center) presents almost no gap function amplitude.

Keywords— Unconventional superconductivity, Matrix Random Phase Approximation, Lifshitz transition

Contents

1 Introduction

The discovery of superconductivity in Mercury, by Heike Kamerlingh Onnes in 1911 (ONNES, 1911), with critical temperature $T_c = 4.15K$, launched one of the most vibrant areas of research in Physics, in the twentieth century. At first, a very slow increase in T_c seemed to indicate that applications would be very scarce (see Fig. 1). However, in 1986, the discovery of superconductivity in the cuprates (LaBaCuO) (BEDNORZ; MÜLLER, 1986), with $T_c = 35K$, started a new era in superconductivity research. As shown in Fig. 1, this started a vertiginous increase in T_c, which has achieved the remarkable value of $T_c = 133K$, measured in the cuprate material $HgBa_2Ca_2Cu_3O_{8+\delta}$ (SCHILLING et al., 1993). These new materials have a *pairing* mechanism (not understood yet) different from that present in the so-called conventional superconductors (the metal elements, for example, with lower T_c), and thus were christened *unconventional* superconductors.

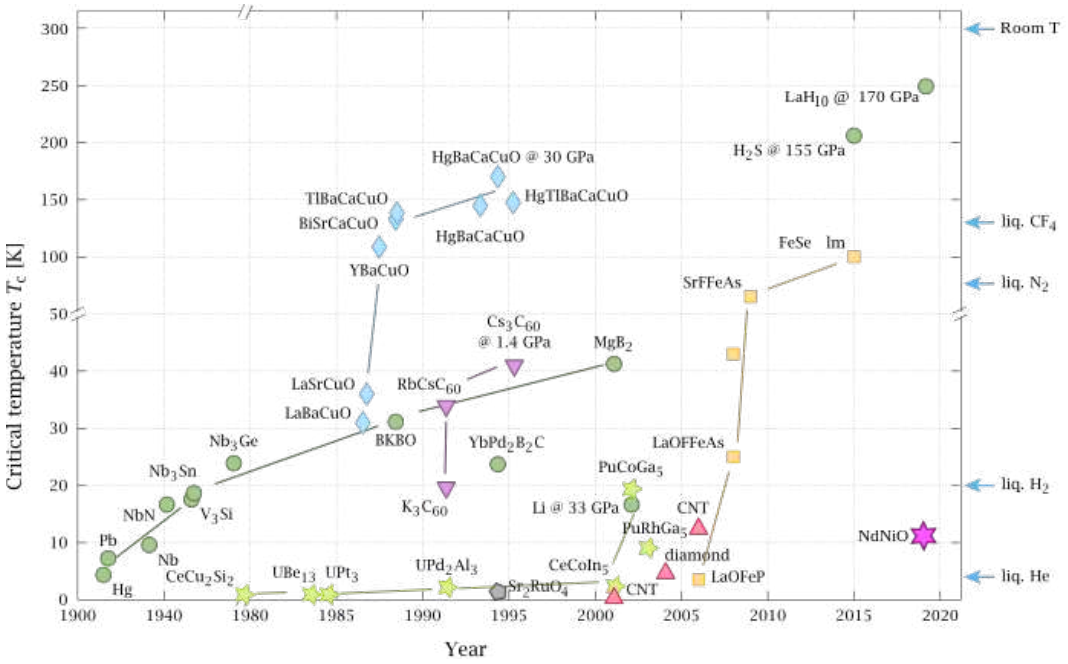

Figure 1 – Schematic description of T_c evolution since 1911, when Hg superconductivity was discovered by Kamerling Onnes. Figure obtained from the Wikipedia entry 'High-temperature superconductivity'.

In this dissertation, focused on unconventional superconductivity, we will explore, using the Matrix Random Phase Approximation (MRPA) (TAKIMOTO; HOTTA; UEDA, 2004; GRASER et al., 2009), the (possible) superconducting properties of the compound LaCrAsO (WANG et al., 2017; PIZARRO et al., 2017) [isostructural to LaFeAsO, which is a member of an extensive family of high-T_c Iron superconductors (SCALAPINO, 2012; DAI; HU; DAGOTTO, 2012; DAGOTTO, 2013)]. The application of the RPA approximation, also called fluctuation exchange (FLEX) approximation, to study superconductivity in the *single*-band Hubbard model (HUBBARD, 1963), was proposed in 1989 by Douglas Scalapino's group (BICK-

ERS; SCALAPINO; WHITE, 1989) right after the discovery of high-T_c superconductivity in the cuprates (BEDNORZ; MÜLLER, 1986). The extension of the RPA method to treat a *multi*-band Hubbard model (appropriate for heavy-fermions (STEWART, 1984) and iron pnictides, thus requiring the use of the *matrix* RPA) was proposed by Takimoto *et al.* (TAKIMOTO; HOTTA; UEDA, 2004) in 2004. Along the years, the community involved in the development of the technique settled in the use of the FLEX acronym to denote *self-consistent* calculations, while the RPA (or MRPA) acronym was reserved to *non-self-consistent* calculations. The Hubbard model is the simplest effective model of fermions with local interactions that is believed by many to describe many of the phases observed in the cuprates (ANDERSON, 1987). In addition, it is believed to exhibit superconductivity arising from purely repulsive interactions (KOHN; LUTTINGER, 1965; MAITI; CHUBUKOV, 2013) and has been extensively applied to explore a variety of unconventional superconducting systems. See Ref. (LONG, 1991), and the following papers in the same volume, for a comprehensive discussion of the Hubbard model.

As mentioned above, in this dissertation, we will use the MRPA *spin-fluctuation pairing scheme* to calculate the *particle-particle scattering vertex* for a multi-band Hubbard model description of LaCrAsO, and, from it, obtain the gap function of the leading superconducting instability of the model. The use of the *matrix* RPA is necessary, since all five Chromium 3d bands cross the Fermi energy in the electronic structure of the Chromium oxide layer (which hosts superconductivity) in LaCrAsO. In the case of the cuprates, like La_2CuO_4, the high-T_c community has long accepted (after much fight...) the single-band Hubbard model as the minimal model to describe it, where one can revert to the use of the simpler *non-matrix* flavor of RPA, which is substantially less costly from the computational point of view, and whose results are considerably simpler to interpret.

What justifies using the RPA and not the Bardeen-Cooper-Schrieffer (BCS) theory (BARDEEN; COOPER; SCHRIEFFER, 1957) to analyze high-T_c superconductors? The BCS theory, in its original variational form, is valid when the typical energies characterizing the superconducting state (critical temperature T_c and gap Δ, for example) are much smaller than all other energy scales entering the problem. The diminutive value of these energy scales (T_c and Δ) is caused by the weakness of the effective attraction between the electrons forming the Cooper pairs (COOPER, 1956). As a result, BCS theory is said to be a weak coupling theory. In cases where this coupling is no longer small (even in conventional superconductors, like Pb and Hg [1]), a 'strong coupling' theory is necessary. In reality, there are a few different theories that incorporate strong coupling interactions, like the Eliashberg theory (MARSIGLIO, 2020) (also called Migdal-Eliashberg theory), or, as in our case, the RPA approximation to calculate the Bethe-Salpeter kernel (MALIK, 2016), which is used to calculate the pairing vertex using quantum field theory [2]. It can be shown that the BCS equations, for an elemental superconductor, obtained via a variational approach (i.e., BCS theory) may also be obtained via this alternative

[1] While the BCS theory result for the ratio $2\Delta(0)/k_B T_c$ is 3.53 [which is the measured value for Al, a BCS superconductor (MATTHIAS; GEBALLE; COMPTON, 1963)], it takes the value 4.3 for Pb (GIAEVER; HART; MEGERLE, 1962) and 4.6 for Hg (BERMON; GINSBERG, 1964).

[2] The Bethe-Salpeter equation treats time-dependent two-particle interactions. Being a many-body problem, its solution has to resort to some approximation, which in our case is the MRPA.

approach based on a temperature-generalized Bethe-Salpeter equation, employing as its kernel the one-phonon propagator (MALIK, 2016). One may view Cooper pairs in the latter approach as being bound together via the 'glue' provided by a single spring. In the case of a non-elemental superconductor (MgB_2, for example, with $T_c = 39K$ (KORTUS, 2007)) a superpropagator is employed as the kernel, thus the Cooper pairs will be bound together by the stronger glue provided by a composite spring. It is this feature that causes T_c enhancement for a non-elemental superconductor. A superpropagator represents the propagation of a weighted superposition of multiple quanta. Thus, a field-theoretic construct exists which may be used in going from the scenario of two electrons bound via the exchange of a single phonon to the scenario where they are bound via the exchange of multiple phonons, that naturally arises in non-elemental superconductors.

Another important question that is relevant to high T_c systems simulated by the Hubbard model is the following. Can superconductivity arise from purely repulsive interactions? That is, without the help of phonons, which originate from outside the Fermi sea. A seminal proposal by Kohn and Luttinger (KOHN; LUTTINGER, 1965) suggests a positive answer. Indeed, their proposal is based on the fact that the combination of charge screening in metals and a discontinuous drop of $n(k)$ (electron occupancy) at the Fermi surface results in an oscillatory potential of the form $cos(2k_F r+\phi)/r^3$. They then posit that "*It is plausible to suppose that, similarly, the effective interaction between the fermions themselves will have a long-range oscillatory part. By taking advantage of the attractive regions, Cooper pairs can form, thus giving rise to superconductivity*". Obviously, regions where the electron density is less than the average will have a net positive charge, generating an attraction between two electrons. It is interesting to reproduce here the first paragraph of this seminal paper (KOHN; LUTTINGER, 1965):

It is the purpose of this note to point out a new mechanism which provides an instability against Cooper-pair formation. We find that a weakly interacting system of fermions cannot remain normal down to the absolute zero of temperature, no matter what the form of the interaction. This mechanism has nothing to do with the conventional electron-phonon attractive interaction in metals, or the long-range attractive van der Waals forces in He^3. It is present even in the case of purely repulsive forces between the particles, and (it) is due to the sharpness of the Fermi surface for the normal system.

One major experimental aspect of high-T_c superconductivity is the almost *universal* presence of an antiferromagnetic (AF) phase close to the superconducting one (see Fig. 2). This is true of the cuprates, iron-pinictides and -chalcogenides, the recently discovered nickelates (PICKETT, 2021), and also true of some heavy fermions and actinides. For a recent review of this particular aspect, please see Ref. (SCALAPINO, 2012). Obviously, as shown in Fig. 2, hole- (or, sometimes, electron-) doping is necessary to bring down the Néel temperature, destroying the Mott insulator phase, and generate a so-called strange metal, thus ushering in the superconducting phase. This fact, the closeness of superconductivity to an AF phase, led many to believe that paramagnons (excitations present in the remaining AF short-range order) would form the 'glue' responsible for Cooper pair formation in heavy-fermions, some organic superconductors (Bechgaard salts), and possibly also in the cuprates. This became known as

the paramagnon spin fluctuation mechanism (SCALAPINO, 1999). The first theory showing the importance of spin fluctuations for superconductivity was proposed by Bob Schrieffer in 1966 (BERK; SCHRIEFFER, 1966), where he showed that paramagnon spin fluctuations could *suppress* superconductivity in nearly-ferromagnetic materials. That result spurred a lot of activity in the field. Indeed, right after Schrieffer's results, it was proposed that paramagnon spin fluctuations provide the p-wave pairing mechanism responsible for superfluidity in He^3 (FAY; LAYZER, 1968; LAYZER; FAY, 1974).

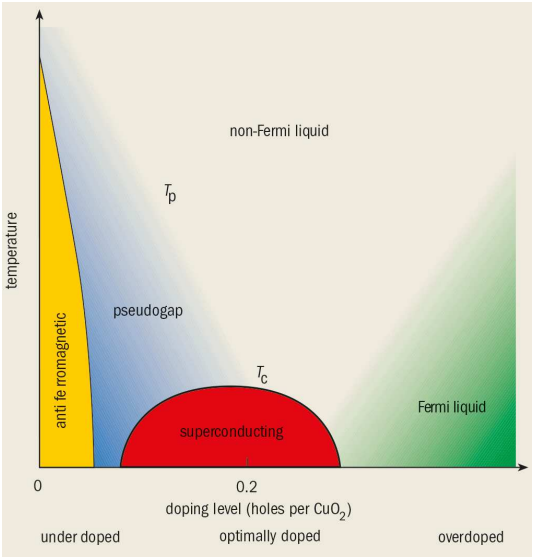

Figure 2 – Schematic phase diagram for the cuprates, showing the presence, at very low hole doping ($\lesssim 0.05$), of an antiferromagnetic phase, associated to a Mott insulator phase (zero doping). After the suppression of magnetic order, a superconducting dome is present, with a maximum transition temperature at optimal doping. (BATLOGG; VARMA, 2000)

It is in that tradition of Cooper pairs formed through paramagnon-exchange that the MRPA technique is presented, and understood, in this dissertation, centered in a Chromium pnictide material.

This dissertation is organized as follows: in Chapter 2 we provide a motivation for the subject analyzed, where we initially situate it in the context of unconventional superconductivity as a whole, providing some historic perspective, including a brief formal analysis of Cooper pair formation and the Bardeen-Cooper-Schrieffer (BCS) theory. In Chapter 3, we present the methods used in this dissertation: the tight-binding (TB) method and the MRPA. The TB method will be developed in the context of Wannier orbitals, obtained through Density Functional Theory (DFT) [3]. In Chapter 4 we present a historical perspective about Chromium-pnictides superconductors and our MRPA results for LaCrAsO. We close with our conclusions and perspectives for future work in Chapter 5. Some of the more technical material is relegated to the Appendices. Despite its extension, we elected to provide the code used, for completeness, in the Appendices.

[3] Although the LaCrAsO TB parameters we used were obtained from the literature (WANG et al., 2017), we developed extensive knowledge on obtaining 'ab-initio' TB parameters via the DFT+Wannier90 strategy. Results for graphene are presented to illustrate that.

2 Superconductivity

2.1 Historic Perspective

In 1957, John Bardeen, Leon Cooper, and John Robert Schrieffer (BCS) (BARDEEN; COOPER; SCHRIEFFER, 1957) proposed a theoretical model that describes pairs of electrons, with opposite momenta and spin, which couple through electron-phonon interaction, to describe the superconducting state of ordinary metals. Superconductivity is the phenomenon in which resistivity vanishes below a critical temperature T_c and magnetic flux is ejected from the material. The BCS theory, where pairing is mediated by phonons, describes the so-called conventional superconductors. Pairing in the so-called unconventional superconductors (HIRSCH; MAPLE; MARSIGLIO, 2015; STEWART, 2017) is believed to be caused by the exchange of spin and/or charge fluctuations between the pairing electrons. Paradoxically, the 'glue' for the pairing (the fluctuations) are caused by the repulsion between the electrons. Indeed, the many (spin and charge) ordered phases present, for example, in the phase diagram of the cuprates (DAGOTTO, 1994), are believed to provide the order parameter, whose fluctuations (paramagnons in the case of spins (SCALAPINO, 2012; WANG et al., 2022)) are the bosons exchanged by the electrons in Cooper pairs. A prominent idea in the field is that spin fluctuations are the unifying concept for all unconventional superconductors (SCALAPINO, 2012).

In 1911, H. K. Onnes carried out experiments measuring the resistivity of Hg at low temperatures, and with these experiments (ONNES, 1911), the first superconductor in history was discovered, with a transition temperature $T_c = 4.2K$(MATTHIAS; GEBALLE; COMPTON, 1963). With the discovery of that new phase of matter, various other metas were found to be superconductors, such as Pb ($T_c = 7.19K$) (MATTHIAS; GEBALLE; COMPTON, 1963), Nb ($T_c = 9.25K$) (WEBB, 1969), etc. However, for a long time, superconductors consisted of a single element, until NbN ($T_c = 16K$) (SHY; TOTH; SOMASUNDARAM, 1973) was discovered to be a superconductor.

The search for other superconductors continued throughout the rest of the 20th century, resulting in the discovery of unconventional superconductors in the 1980s. In the 21st century, experiments have not stopped. In 2001, the superconductor MgB_2 ($T_c = 39K$) (NAGAMATSU et al., 2001) was synthesized, and Iron superconductors were discovered (SCALAPINO, 2012).

2.2 BCS Theory

In the following subsections, we will summarize the basis and formalism of the BCS theory.

2.2.1 Cooper pairs

Although the electrostatic interaction between two electrons is repulsive, it was long suspected that ionic vibrations of the lattice can produce a net attractive potential. It was Leon Cooper who first showed (COOPER, 1956) that an attractive interaction, no matter how weak it is, in the presence of a Fermi Sea, can generate a bound state in a pair of electrons $|\vec{k}_\uparrow, -\vec{k}_\downarrow\rangle$ added to the system. Thus, electrons on the Fermi surface of a metal will pair up to form bound states, so that the ground state energy is reduced. Therefore, the Fermi surface is no longer stable, since more electrons may pair up, to form Cooper pairs, and lower the system's energy. The metal may then transition from the so-called normal state to the superconducting state, which is a 'coherent' superposition of Cooper pairs.

A 'hand waving' description of Cooper pairing goes along the following lines: A free electron in a metal produces an attractive interaction in the nearby positively charged lattice ions. As the ion mass is many times greater than the electron mass, the ion velocity is much less than the electron velocity. Thus, after the electron has already moved out of the lattice region it perturbed, a net concentration of positive charge remains, generating an attractive potential for other nearby electrons. It turns out that this potential is more effective in attracting electrons of opposite momentum and spin to the electron that caused the lattice distortion in the first place, thus the effective potential is responsible for the formation of the Cooper pair.

In the following, we provide a heuristic description of the Cooper pair instability, based on Ref. (MANGIN; KAHN, 2016).

2.2.1.1 Single-particle analysis

We will consider the Hamiltonian H_0, written in its eigenstate basis, denoted $|1\rangle, |2\rangle, |3\rangle$ and $|4\rangle$, whose eigenvalues are degenerate, i.e., $\varepsilon_i = \varepsilon$, for all i. Next, we add an potential $\hat{V}$ to the system, obtaining a perturbed Hamiltonian $H = H_0 + \hat{V}$, where $\langle i|\hat{V}|j\rangle = \hat{V}_{ij} = -V$ (where $V > 0$), and then calculate the eigenvalues and eigenstates of the perturbed Hamiltonian, whose eigenvalue equation in matrix form is given by [1]

$$\begin{bmatrix} \varepsilon - V - E & -V & -V & -V \\ -V & \varepsilon - V - E & -V & -V \\ -V & -V & \varepsilon - V - E & -V \\ -V & -V & -V & \varepsilon - V - E \end{bmatrix} \begin{bmatrix} c_1 \\ c_2 \\ c_3 \\ c_4 \end{bmatrix} = \begin{bmatrix} 0 \\ 0 \\ 0 \\ 0 \end{bmatrix}. \tag{2.1}$$

Thus, the characteristic equation is given by

$$\begin{aligned} E^4 + (4V - 4\varepsilon)E^3 + (6\varepsilon^2 - 12V\varepsilon)E^2 - (4\varepsilon^3 - 12V\varepsilon^2)E + (\varepsilon^4 - 4V\varepsilon^3) &= 0, \\ (E - \varepsilon)^3(4V - (\varepsilon - E)) &= 0. \end{aligned} \tag{2.2}$$

From this expression, we obtain four eigenenergies, three of which are degenerate, $E_\beta = E_\gamma = E_\delta = \varepsilon$, and one lower than the others, $E_\alpha = \varepsilon - 4V$. The eigenvector associated with the lowest

[1] Note that the perturbation is taken as being such that, besides lowering the energy of each H_0 eigenstate, it also 'scatters' an electron from any eigenstate to any other eigenstate, with the same amplitude $(-V)$. As will become clear soon, this is essential for Cooper-pair formation.

energy is given by a symmetric linear combination of the all the H_0 eigenstates,

$$|\alpha\rangle = \frac{1}{\sqrt{4}}[|1\rangle + |2\rangle + |3\rangle + |4\rangle].$$

Thus, it is the gain in energy obtained by phase-space delocalization that produces a state with lower energy than the others, as the three other eigenstates are less delocalized than $|\alpha\rangle$, since they are linear combinations of just two original eigenstates [2].

Now, consider the generalized case, where the Hamiltonian H_0 has N eigenstates with energy ε and we add, as above, a scattering potential $\hat{V}$ to the system. As a result, we get $(N-1)$ degenerate states with energy ε and one state with energy $\varepsilon - NV$. The lowest energy eigenstate $|\alpha\rangle$, which we call a bound state, is again a symmetric linear combination of the N eigenstates of H_0.

We can also consider another type of generalization. We will assume that the eigenstates of H_0 are non-degenerate, where $\varepsilon_1 < \varepsilon_2 < \varepsilon_3 < \varepsilon_4$, and add the same scattering potential $\hat{V}$ to the system. We have to solve four equations, given by

$$\frac{c_i}{V} = \frac{c_1 + c_2 + c_3 + c_4}{\varepsilon_i - E}, \tag{2.3}$$

where $i \in [1, 4]$. Summing all four equations, and simplifying, we obtain the relation

$$\frac{1}{V} = \sum_{i=4}^{4} \frac{1}{\varepsilon_i - E}. \tag{2.4}$$

Figure 3 shows the possible solutions to Eq. (2.4), where the perturbed eigenenergies are indicated by red-dots. From it, we see that, again, there is one (and only one) eigenenergy that is considerably lower than the lowest of the original ϵ_i. The eigenstate associated to this lowest energy is similar to the simplified case described above. Now, all coefficients are still positive, but they obey the inequalities $c_1 > c_2 > c_3 > c_4 > 0$,

$$|\alpha\rangle = c_1|1\rangle + c_2|2\rangle + c_3|3\rangle + c_4|4\rangle.$$

Thus, phase space delocalization is still the mechanism that lowers the energy of the $|\alpha\rangle$ state. However, a balance has to be achieved, where states with higher unperturbed energy should contribute less to the bound state.

2.2.1.2 System of electron pairs

We will now consider a two-electron system, where there are four single-particle states, two with energy ε ($|1\rangle \equiv |\vec{k}_\uparrow\rangle$ and $|2\rangle \equiv |-\vec{k}_\downarrow\rangle$) and two with energy ε' ($|3\rangle \equiv |\vec{k}'_\uparrow\rangle$ and $|4\rangle \equiv |-\vec{k}'_\downarrow\rangle$),

[2] It is very transparent that it is the form of the perturbation $\hat{V}$, which scatters equally each H_0 eigenstate into each other, with a *negative* matrix element $\hat{V}_{ij} = -V$, that results in the *symmetric* $|\alpha\rangle$ state with equal participation of all the unperturbed eigenstates.

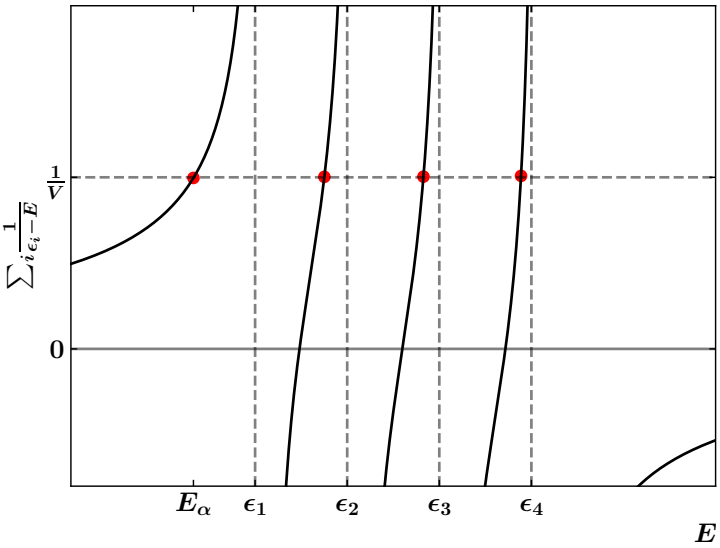

Figure 3 – Graphical solution of relation (2.4). The red dots indicate the eigenenergies, where the leftmost one corresponds to E_α, the bound state. It is clear that, as V increases (and thus $1/V$ decreases), E_α decreases.

where $\varepsilon < \varepsilon'$. As we are considering a two-particle system, the basis of the total Hamiltonian must be modified, since the quantum system must be described by $|j, j'\rangle$ states, where $j, j' \in [1, 4]$. Two-electron states with opposite momenta and spin are the ones that are coupled by the electron-phonon interaction (BARDEEN; COOPER; SCHRIEFFER, 1957). Note that, with the single-particle states just defined above, there are only two possible two-electron states that satisfy the condition of opposite momenta and spin, viz., ($|1, 2\rangle = |\vec{k}_\uparrow, -\vec{k}_\downarrow\rangle$ and $|3, 4\rangle = |\vec{k}'_\uparrow, -\vec{k}'_\downarrow\rangle$), with energies 2ε and $2\varepsilon'$, respectively. We will call them pair-states. On the other hand, there are four two-electron states that do not satisfy this condition, viz., ($|1, 3\rangle = |\vec{k}_\uparrow, \vec{k}'_\uparrow\rangle$, $|1, 4\rangle = |\vec{k}_\uparrow, -\vec{k}'_\downarrow\rangle$, $|2, 3\rangle = |-\vec{k}_\downarrow, \vec{k}'_\uparrow\rangle$, and $|2, 4\rangle = |-\vec{k}_\downarrow, -\vec{k}'_\downarrow\rangle$), with energy $\varepsilon + \varepsilon'$. Now, we add the $\hat{V}$ perturbation (electron-phonon coupling), however, as remarked above, the scattering potential only operates on the pair states. Schematically, we represent the scattering caused by the V potential by Fig. 4, where a pair state close to the Fermi energy is scattered into another pair state.

Based on the considerations in the above paragraph, the total Hamiltonian $H = H_0 + \hat{V}$ has a diagonal block, consisting of a 4×4 matrix with $\varepsilon + \varepsilon'$ diagonal matrix-elements, and a 2×2 matrix, involving the pair-states, given by

$$H^{2\times 2}_{\text{pair}} = \begin{pmatrix} 2\varepsilon - V & -V \\ -V & 2\varepsilon' - V \end{pmatrix}, \tag{2.5}$$

where, as the reader may already anticipate, it is crucial for the electron-phonon interaction to be also active in *scattering* one pair-state into another, as indicated by the off-diagonal matrix elements in Eq. (2.5).

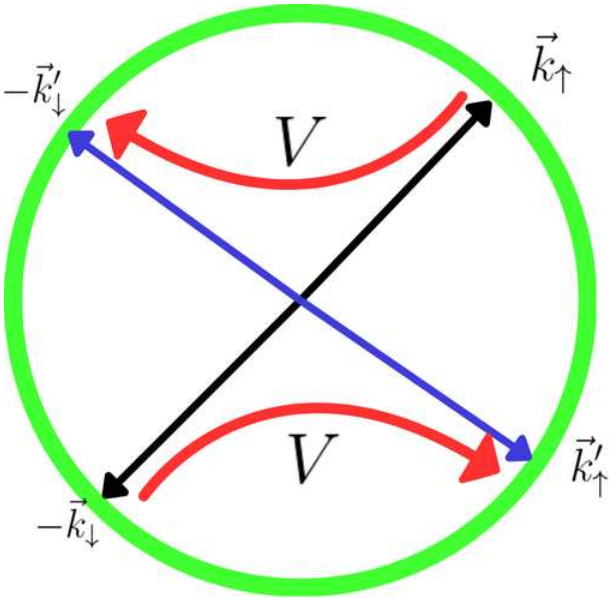

Figure 4 – Representation of the scattering of pair states via a V potential. The green circle represents the Fermi surface.

The $H^{2\times2}_{\text{pair}}$ eigenenergies, in the pair-state subspace, are given by

$$E_{\text{pair}} = [\varepsilon + \varepsilon' - V] \pm \sqrt{(\varepsilon - \varepsilon')^2 + V^2}.$$

Thus, the introduction of the electron-phonon coupling results in three types of eigenstates: a bonding state, i.e., a quantum state with the lowest energy, its corresponding antibonding state, and the $\varepsilon + \varepsilon'$ states, which do not involve pair-states. In the next subsection, we will generalize the procedure just outlined, by considering a pair of electrons added to a metal.

2.2.1.3 Cooper Pair: Bound state

We will consider a metal at temperature $T = 0K$, in which the states below the Fermi energy ε_F are filled. Then, we will assume that two *extra* electrons are added, with energy ε_F, and consider all the other electrons as being frozen. As the BCS pairing-interaction takes place via phonon mediation, the scattering of these two electrons between two pair-states, $|\vec{k}_\uparrow, -\vec{k}_\downarrow\rangle$ and $|\vec{k}'_\uparrow, -\vec{k}'_\downarrow\rangle$, can only take place inside the energy interval $\varepsilon_F < \varepsilon_{\vec{k}} < \varepsilon_F + \hbar\omega_D$, where $\hbar\omega_D$ is the Debye energy (the characteristic energy of the phonon spectra for the metal of interest). Additionally, we redefine the energy of a free electron in a $|\vec{k}\rangle$ state, taking as reference the Fermi energy ε_F, as

$$\begin{aligned} \xi_{\vec{k}} &= \varepsilon_{\vec{k}} - \varepsilon_F = \frac{\hbar^2}{2m}(k^2 - k_F^2), \\ \xi_{\vec{k}} &\cong \frac{\hbar^2 k_F}{m}(k - k_F), \end{aligned} \tag{2.6}$$

where the approximation $k + k_F = 2k_F$ was made in Eq. (2.6), since $\hbar\omega_D \ll \varepsilon_F$. Once we add the electron-phonon interaction, i.e., a perturbation that lowers the energy of the pair-states *and* generates scattering between them, we will have a situation identical to that in Eqs. (2.1) and

(2.5). Thus, we expect to obtain a bound state with energy E_α, which can be obtained via an equation similar to Eq. (2.4), given by

$$\frac{1}{V} = \sum_{k_F}^{k_c} \frac{1}{2\xi_{\vec{k}} - E_\alpha}, \tag{2.7}$$

where $\hbar^2 k_c^2/2m = \varepsilon_F + \hbar\omega_D$. If we consider that there is a continuum of accessible pair-states, we can transform the sum into an integral in energy, given by

$$\frac{1}{V} = \int_0^{\hbar\omega_D} \rho(\varepsilon) \frac{d\varepsilon}{2\varepsilon - E_\alpha}, \tag{2.8}$$

where $\rho(\varepsilon)$ is the density of states per volume unit and E_α is the bound-state energy. If we consider that the integration interval is small, we may consider the density of states as a constant, calculated at the Fermi energy, $\rho(\varepsilon) \Rightarrow \rho(\varepsilon_F)$. Thus, the integral becomes trivial, and we obtain

$$\frac{1}{V} = \frac{\rho(\varepsilon_F)}{2} \ln\left[1 - \frac{2\hbar\omega_D}{E_\alpha}\right]. \tag{2.9}$$

Using the fact that $E_\alpha \ll \hbar\omega_D$, we may neglect the 1 in the ln argument and the approximate analytical expression for E_α is given by

$$E_\alpha = -2\hbar\omega_D e^{-2/V\rho(\varepsilon_F)}, \tag{2.10}$$

where we see that the bound state energy is proportional to the phonon energy scale $\hbar\omega_D$. Furthermore, E_α decreases exponentially with the product of the effective potential V and the density of states at the Fermi energy $\rho(\varepsilon_F)$.

We may define the binding energy $E_b = -E_\alpha$ as the lowering of the two extra electrons energy by their association to form a Cooper pair, which, as already discussed above, is delocalized over the available pair-states above the Fermi surface. Consequently, given two electrons with energy ε_F and at a sufficiently low temperature, if an attractive potential is applied, *which scatters pair-states among themselves with amplitude* $-V$, a so-called Cooper pair is formed, with a binding energy given by the negative of Eq. (2.10).

2.2.2 Many Cooper pairs

While Cooper considered only a single pair of electrons (COOPER, 1956), the theory of Bardeen, Cooper and Schrieffer (BCS theory) considered that many electrons in the solid could form bonded pairs in the ground state. Their effective Hamiltonian is given by

$$H = \sum_{\vec{k}\sigma} \xi_{\vec{k}} c^\dagger_{\vec{k}\sigma} c_{\vec{k}\sigma} + \frac{1}{N} \sum_{\vec{k}\vec{k}'} V_{\vec{k}\vec{k}'} c^\dagger_{\vec{k}\uparrow} c^\dagger_{-\vec{k}\downarrow} c_{-\vec{k}'\downarrow} c_{\vec{k}'\uparrow}, \tag{2.11}$$

where $c^\dagger_{\vec{k}\sigma}$ ($c_{\vec{k}\sigma}$) are electron creation (annihilation) operators with momentum $\vec{k}$ and spin σ [3] and $\xi_{\vec{k}} = \varepsilon_{\vec{k}} - \mu$, where μ is the chemical potential. The second term in the Hamiltonian describes

[3] For more details about second quantization, please see Appendix A.

the scattering from the pair-state $|\vec{k}'_\uparrow, -\vec{k}'_\downarrow\rangle$ to $|\vec{k}_\uparrow, -\vec{k}_\downarrow\rangle$. Furthermore, in BCS theory we can consider a simplified potential, where the scattering potential is given by

$$V_{\vec{k}\vec{k}'} = \begin{cases} -V & \text{if } \varepsilon_F - \hbar\omega_D < \varepsilon_{\vec{k}} \text{ and } \varepsilon_{\vec{k}'} < \varepsilon_F + \hbar\omega_D \\ 0 & \text{otherwise.} \end{cases}$$

To solve Hamiltonian (2.11), BCS performs a decoupling via the mean-field approximation

$$c^\dagger_{\vec{k}\uparrow} c^\dagger_{-\vec{k}\downarrow} c_{-\vec{k}\downarrow} c_{\vec{k}\uparrow} \cong \langle c_{-\vec{k}\downarrow} c_{\vec{k}\uparrow}\rangle c^\dagger_{\vec{k}\uparrow} c^\dagger_{-\vec{k}\downarrow} + \langle c^\dagger_{\vec{k}\uparrow} c^\dagger_{-\vec{k}\downarrow}\rangle c_{-\vec{k}\downarrow} c_{\vec{k}\uparrow} - \langle c_{-\vec{k}\downarrow} c_{\vec{k}\uparrow}\rangle \langle c^\dagger_{\vec{k}\uparrow} c^\dagger_{-\vec{k}\downarrow}\rangle,$$

and defines the gap function as

$$\Delta_{\vec{k}} = -\frac{1}{N} \sum_{\vec{k}'} V_{\vec{k}\vec{k}'} \langle c_{-\vec{k}'\downarrow} c_{\vec{k}'\uparrow}\rangle. \tag{2.12}$$

Once we have the Hamiltonian written in terms of the gap function in the mean-field approximation, we can perform the Bogoliubov transformation. That transformation allows us to describe the system using Bogoliubov quasiparticles, which are linear combinations of electrons and holes. The transformed Hamiltonian is given by

$$H_{\text{BCS}} = E_{\text{BCS}} + \sum_{\vec{k}\sigma} E_{\vec{k}} \gamma^\dagger_{\vec{k}\sigma} \gamma_{\vec{k}\sigma}, \tag{2.13}$$

where $\gamma_{\vec{k}\sigma}$ are fermionic operators, and $E_{\vec{k}} = \sqrt{\xi^2_{\vec{k}} + |\Delta_{\vec{k}}|^2}$. We can determine the gap function in terms of the Bogoliubov operators (2.14), considering $\langle \gamma^\dagger_{\vec{k}'\uparrow} \gamma_{\vec{k}'\uparrow}\rangle = n_F(E_{\vec{k}'})$, $\langle \gamma_{-\vec{k}'\downarrow} \gamma^\dagger_{-\vec{k}'\downarrow}\rangle = 1 - n_F(E_{\vec{k}'})$ and $n_F(E_{\vec{k}'}) = 1/(1 + e^{\beta E_{\vec{k}'}})$.

$$\Delta_{\vec{k}} = -\frac{1}{N} \sum_{\vec{k}'} V_{\vec{k}\vec{k}'} \frac{\Delta_{\vec{k}'}}{2E_{\vec{k}'}} \Big(1 - 2n_F(E_{\vec{k}'})\Big) \tag{2.14}$$

We will take a particular case, where the gap function does not depend on $\vec{k}$ ($\Delta_{\vec{k}} \to \Delta$), also called the s-wave[4]. To realize the case, the potential must not depend on $\vec{k}$ ($V_{\vec{k}\vec{k}'} = -V_0$), so we have

$$1 = \frac{V_0}{N} \sum_{k<k_D} \frac{1}{2E_k} \tanh\left(\frac{E_k}{2k_B T}\right) \Rightarrow 1 = V_0 \int_{-\hbar\omega_b}^{\hbar\omega_b} d\varepsilon \frac{\rho(\varepsilon)}{\sqrt{\varepsilon^2 + \Delta^2}} \tanh\left(\frac{\sqrt{\varepsilon^2 + \Delta^2}}{2k_B T}\right) \tag{2.15}$$

At the limit $\Delta \to 0$, we can determine the critical temperature (T_c), given by

$$\begin{aligned} \frac{1}{V_0 \rho_F} &= \int_0^{\hbar\omega_D} \frac{d\varepsilon}{\varepsilon} \tanh\left(\frac{\varepsilon}{2k_B T_c}\right) \\ T_c &= \frac{2\hbar\omega_D e^{\gamma'}}{\pi k_B} e^{-1/V_0\rho_F}. \end{aligned} \tag{2.16}$$

For the first time, a microscopic theory explains the low critical temperatures of the superconducting phase (BARDEEN; COOPER; SCHRIEFFER, 1957), due to exponential

[4] The most general treatment for s-wave is when the function has no nodes.

dependence. It should also be noted that regardless of the weakness of the V_0 coupling, the theory predicted a superconducting phase transition.

Therefore, the lowest energy of the system is due to the attractive potential between electrons of opposite momenta and spin, and so the state corresponding to this energy is a delocalized state in all accessible pair-states $|\vec{k}_\uparrow, -\vec{k}_\downarrow\rangle$ close to the Fermi level. For Cooper pairs, the pair-states have a probability of occupation ($|v_{\vec{k}}|^2$) given by

$$|v_{\vec{k}}|^2 = \frac{1}{2}\Big[1 - \frac{\xi_{\vec{k}}}{\sqrt{\xi_{\vec{k}}^2 + |\Delta|^2}}\Big], \tag{2.17}$$

while the probability of being unoccupied is $|u_{\vec{k}}|^2 = 1 - |v_{\vec{k}}|^2$, Fig 5.

Due to the nature of Cooper pair formation, the occurrence of scattering between pair-states at the Fermi energy is fundamental to the establishment of the superconducting ground state. Indeed, this can be understood by noticing that the superconducting gap Δ is given by

$$\Delta = V \sum_{\vec{k}} \chi_{\vec{k}} = V \sum_{\vec{k}} v_{\vec{k}} u_{\vec{k}}. \tag{2.18}$$

where $\chi_{\vec{k}} = u_{\vec{k}} v_{\vec{k}}$ (see solid black curve in Fig. 5) measures the participation of each pair-state in gap formation, being $|v_{\vec{k}}|^2$ the probability for pair-states to be *occupied* and $|u_{\vec{k}}|^2 = 1 - |v_{\vec{k}}|^2$ the probability for pair-states to be *unoccupied*. Thus, in the hypothetical situation where all pair-states below the Fermi energy are *fully* occupied (red dash-dotted curve in Fig. 5), the superconducting gap Δ vanishes, since $u_{\vec{k}} v_{\vec{k}} = 0$ for all $\vec{k}$. Therefore, a pair-state is effective in participating in the formation of the superconducting ground state if it can be both the origin of a scattering event ($|v_{\vec{k}}|^2 > 0$, i.e., partially occupied) and the destination of a scattering event ($|u_{\vec{k}}|^2 < 1$, i.e., partially unoccupied).

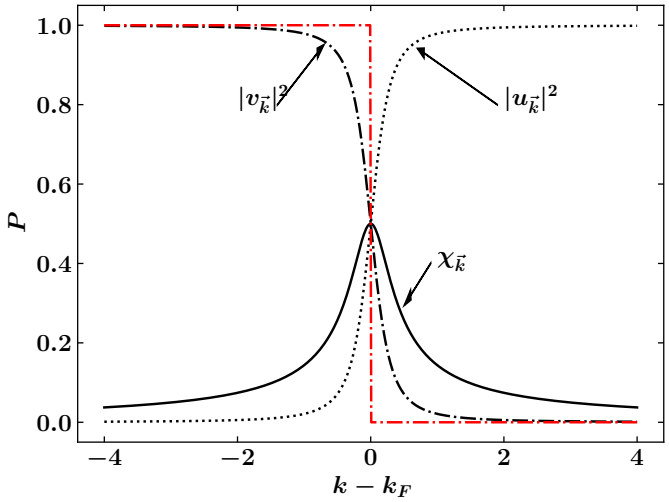

Figure 5 – Probability for pair-states to be occupied ($|v_{\vec{k}}|^2$, black dash-dotted curve) and unoccupied ($|u_{\vec{k}}|^2 = 1 - |v_{\vec{k}}|^2$, black dotted curve). $\chi_{\vec{k}} = u_{\vec{k}} v_{\vec{k}}$ measures the participation of each pair-state in gap formation, i.e., $\Delta = \sum_{\vec{k}} \chi_{\vec{k}}$. The red dash-dotted curve indicates a hypothetical situation, with fully occupied pair-states below the Fermi energy, that results in a vanishing gap, since the product $u_{\vec{k}} v_{\vec{k}}$ vanishes for all $\vec{k}$. Adapted from Ref. (MANGIN; KAHN, 2016).

3 Methods

In this chapter we will present the techniques used in the multiorbital RPA calculation, in particular a brief explanation of the tight-binding model, the essence of RPA and the study of the convergence of the RPA calculation.

3.1 Tight-Binding Method

When working with solids, a priori, we need to consider all the atomic orbitals of each chemical element and their interactions. This is the approach taken by Density Functional Theory (DFT), using the Kohn-Sham approximation to treat the electron interactions. The Kohn-Sham approximation (KOHN; SHAM, 1965; ENGEL; DREIZLER, 2011) maps the complex interacting electron system onto a system of non-interacting electrons moving in an effective potential, which includes the effects of electron exchange and correlation. An alternative approach is to treat the solid at a qualitative level, by using a tight-binding (TB) approach, which we will describe in this chapter. The great advantage of the TB method is that it allows the study of model Hamiltonians (which describe strong correlations between electrons, like the Hubbard model), beyond the mean-field level.

If we consider a collection of neutral atoms isolated by a few centimeters, the wave function of the electrons of each element can be well described as atomic wave functions. However, in order to form a solid, the distance between the atoms must be reduced, and as a result, the electronic levels will be modified due to the interaction among the electrons. In other words, for the electrons closest to the nucleus, the interactions between the electrons of neighboring atoms can be almost negligible, so their wave functions remain the same as the electronic levels of an isolated atom. As for the electrons in the valence layer, the interactions with neighboring atoms are more relevant and their wave functions can be modified. The TB approach deals precisely with this description, where the wave functions of the electrons in the valence layer are overlapped with those of neighboring atoms, and the electrons in the inner layers remain atomic in description.

We will now consider a non-interacting fermionic system[1] whose Hamiltonian is given by

$$H_{\text{free}} = \sum_{\vec{k},\sigma} \epsilon_{\vec{k}}^{\text{free}} c_{\vec{k}\sigma}^{\dagger} c_{\vec{k}\sigma}, \tag{3.1}$$

where

$$\epsilon_{\vec{k}}^{\text{free}} = \frac{p^2}{2m} = \frac{\hbar^2 k^2}{2m}$$

is the energy dispersion. In position space, the Hamiltonian becomes

$$H_{\text{free}} = \frac{1}{N} \sum_{ij\sigma} \sum_{\vec{k}} \epsilon_{\vec{k}}^{\text{free}} e^{i\vec{k}\cdot(\vec{r}_i - \vec{r}_j)} c_{i\sigma}^{\dagger} c_{j\sigma}, \tag{3.2}$$

[1] For more details about the second quantization, please see Appendix A.

and we will define the hopping amplitude as

$$t_{ij} \equiv \frac{1}{N} \sum_{\vec{k}} \epsilon_{\vec{k}}^{\text{free}} e^{i\vec{k}\cdot(\vec{r}_i - \vec{r}_j)}. \tag{3.3}$$

If we consider that the non-interacting fermions are in a Bravais lattice with well-localized potentials at each site, then the scattering energy changes, and consequently the hopping amplitude also changes. As a result, the fermions tend to be more localized on the lattice sites. Thus, the tight-binding approximation is given by

$$t_{ij} = \begin{cases} -t, & \text{if } i \text{ and } j \text{ are nearest neighbors} \\ 0, & \text{otherwise,} \end{cases}$$

and the tight-binding Hamiltonian is given by

$$H_{\text{TB}} = -t \sum_{\langle ij \rangle, \sigma} (c_{i\sigma}^{\dagger} c_{j\sigma} + c_{j\sigma}^{\dagger} c_{i\sigma}), \tag{3.4}$$

where $\langle ij \rangle$ signifies that we are considering only nearest-neighbor hoppings.

In the DFT approximation, the wave functions are maybe described by Bloch functions, the same ones that the TB approximation is based on, where the atomic wave functions are known as Wannier functions. These bands can be defined for any type of electronic band, regardless of whether the TB approximation works. The difference is that if the band to be described is not of the TB type, the Wannier functions will not be of the atomic orbital type. In Appendix C we demonstrate a case where the DFT bands of a porphyrin-type molecule embedded in graphene were calculated, and from the DFT bands, the Wannierization was carried out, i.e., the Wannier functions that best describe the bands of the material were calculated.

In order to exemplify how to obtain the hopping parameters for a physical system, we will consider a unit cell with 2 carbon atoms based on hexagonal symmetry, and perform the DFT calculation using the Quantum Espresso software (GIANNOZZI et al., 2009; GIANNOZZI et al., 2017), and obtain the band structure, FIG. 6, and the wave functions for graphene. Based on these results, the wave functions were analyzed, in which the orbitals used to reproduce the DFT bands were s, p_x, p_y and p_z (for the first carbon atom in the base), and p_z (for the second carbon in the base). In addition to reproducing the band structure curves, the hopping parameters up to the eighth neighbour were also calculated. To demonstrate the result, the on-site hopping matrix is given by

$$H_{\text{on site}}^{\text{GR}} = \begin{pmatrix} -12.94691 & -1.99017 & -1.99017 & 0.00000 & 0.00000 \\ -1.99017 & -12.94691 & -1.99017 & 0.00000 & 0.00000 \\ -1.99017 & -1.99017 & -12.94691 & 0.00000 & 0.00000 \\ 0.00000 & 0.00000 & 0.00000 & -1.80484 & -2.87254 \\ 0.00000 & 0.00000 & 0.00000 & -2.87254 & -1.80484 \end{pmatrix}, \tag{3.5}$$

where the diagonal elements are the orbital energies of the orbitals used in the wannierization, following the order $\mathbf{C_A}$:s, p_x, p_y, p_z, and $\mathbf{C_B}$:p_z, while the off-diagonal elements are hopping between the orbitals on the site itself, which is the description of the π and σ bonds of graphene.

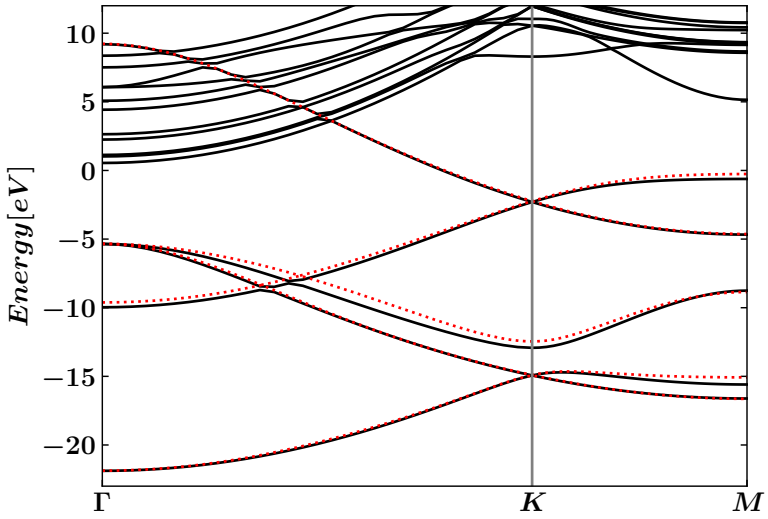

Figure 6 – DFT (black curves) and Wannier (red curves) band structure for graphene. At the K point, both curves reproduce the Dirac cone characteristic of graphene.

3.2 Matrix Random Phase Approximation Method

The MRPA method (TAKIMOTO; HOTTA; UEDA, 2004; GRASER et al., 2009) is a many-body approach (BICKERS; SCALAPINO; WHITE, 1989) to study unconventional superconductivity in materials whose band structure, around the Fermi level, depends on two or more orbitals. The method takes into account spin and charge fluctuations, treated at the RPA level, which may result in electron pairing (SCALAPINO, 1995; SCALAPINO, 1999; MORIYA; UEDA, 2000). Details of the development of some of the equations shown in this section can be found in the review article (BICKERS; SCALAPINO, 1989).

As shown in Fig. 7, the starting point is to write the Hamiltonian that includes multiple orbitals for both the kinetic energy, where the tight-binding parameters are obtained via DFT+Wannier90 calculation (Eq. 4.1), and the Coulomb interaction terms, described by the intra-orbital, inter-orbital, exchange interaction, and pair hopping terms (Eq.(4.2)).

The next step in the method is to calculate the electronic *interacting* susceptibility of the system, both for the spin and charge sectors. Those susceptibilities describe the response of the physical system to small variations in spin and/or charge, and can indicate a phase instability, such as a transition to an ordered magnetic state, a charge-ordered state, or the formation of a superconducting state (SCALAPINO, 1995; SCALAPINO, 1999; MORIYA; UEDA, 2000). Those interacting susceptibilities are obtained, through MRPA (Eqs. (3.11) and (3.12)), from the non-interacting susceptibility χ_0 (Eq. (3.10)).

Finally, the last stage of the method is the calculation of the pairing vertex at the Fermi

surface points k and k' ($\Gamma(k,k')$ in Eq. (3.19)), followed by the diagonalization of the integrand in Eq. (3.21). Those Fermi surface points, k and k', form a set of discrete pair scattering points (see, for example, Fig. 7), which transform a continuous integrand function into a discrete set of scattering events. This way, the indexes of the matrix to be diagonalized may be defined. The larger the number of k and k' points, the better is the convergence to the continuum (see convergence analysis in section 3.2.6). In the calculation of the pairing vertex, the effective interactions (spin and charge fluctuations) that mediate the scattering of Cooper pairs were taken into account via MRPA, for singlet- and triplet-pairing in Eqs. (3.17) and (3.18), respectively. As shown in Eq. (3.21), the eigenvalues of the pairing vertex (denoted λ_α, whose highest value is normalized to 1) define the strength of the different pairing symmetries, which can be assessed by determining the irreducible representation of the corresponding eigenvector g_α (which describes the value of the gap function at the Fermi surface).

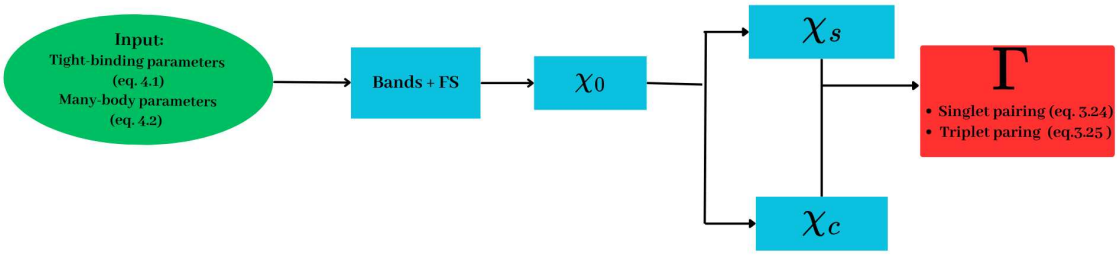

Figure 7 – Schematic representation of the stages involved in the MRPA method. The tight-binding Hamiltonian is diagonalized, producing the bands and the Fermi surface (FS), then, the non-interacting susceptibility χ_0 is calculated, Eq. (3.10). With it, the spin and charge interacting susceptibilities (χ_s and χ_c, Eqs. (3.14) and (3.13), respectively) are calculated at the RPA level. Using those interacting susceptibilities, calculated at each point k and k' of the Fermi surface, we can calculate the pairing vertex (Γ) for singlet- and triplet-pairing, Eqs. (3.17) and (3.18), respectively.

3.2.1 Fermi Surface

By construction, the Fermi surface will be given by the set of $\vec{k}_F$ points, where $E(\vec{k}_F) = \mu$, i.e., the Fermi surface defines the boundary in momentum space where the energy of the electrons is equal to the Fermi energy.

There are a few ways of calculating the Fermi surface, and the most widely used is the ab-initio method such as DFT, where it is possible to determine the dispersion relation $E(\vec{k})$ with high precision. In our case, we have the tight-binding parameters derived from the DFT calculation, so we developed a code in FORTRAN90, where we calculate the Fermi surface for each doping of interest, please see Appendix B.1 for more details. Experimentally, it is possible to map the Fermi surface using the *angle-resolved photoemission spectroscopy* (ARPES) technique (HüFNER, 2003).

3.2.2 Non-Interacting Susceptibility - χ_0

Susceptibility is, by definition, the response of a physical system when an external disturbance is applied. In particular, when we neglect the contributions of Coulomb interactions, we are working with the non-interacting susceptibility χ_0. The non-interacting susceptibility can also be called Lindhard susceptibility, because in 1954 physicist Jens Lindhard described the electronic susceptibility of a gas of free electrons (LINDHARD, 1954; ASHCROFT; MERMIN, 1976).

The spin operator for an orbital s is defined as

$$\vec{S}_s(q) = \frac{1}{2}\sum_{k,\alpha\beta} d^{\dagger}_{s\alpha}(k+q)\vec{\sigma}_{\alpha\beta}d_{s\beta}(k), \tag{3.6}$$

where α and β are spin indices. We can calculate the spin susceptibility from the Matsubara spin-spin correlation function (GRASER et al., 2009)

$$[\chi^{RPA}_{\text{spin}}]^s_t = \frac{1}{3}\int_0^{\beta} d\tau e^{i\omega\tau}\langle T_\tau \vec{S}_s(q,\tau)\vec{S}_s(-q,0)\rangle \tag{3.7}$$

for τ being the imaginary time and ω a Matsubara frequency. On the other hand, we can define the Fourier component of the charge density for the s orbital as being

$$n_s(q) = \sum_{k,\alpha\beta} d^{\dagger}_{s\alpha}(k+q)d_{s\beta}(k)\delta_{\alpha\beta}. \tag{3.8}$$

In the same way, we can calculate the charge susceptibility by

$$[\chi^{RPA}_{\text{charge}}]^s_t(q,i\omega) = \int_0^{\beta} d\tau e^{i\omega\tau}\langle T_\tau n_s(q,\tau)n_s(-q,0)\rangle \tag{3.9}$$

In the non-interacting and more general case, the non-interacting susceptibility can be written as

$$(\chi_0)^{pq}_{st}(q,\omega) = -\frac{1}{N}\sum_{k,\mu\nu}\frac{a^s_\mu(k)a^{p*}_\mu(k)a^q_\nu(k+q)a^{t*}_\nu(k+q)}{\omega + E_\nu(k+q) - E_\mu(k) + i0^+}[f(E_\nu(k+q)) - f(E_\mu(k))] \tag{3.10}$$

where $a^s_\mu(k)$ are elements of the matrix that connect the orbital and the band spaces, i.e., they are the components of the eigenvectors resulting from the diagonalization of the initial Hamiltonian. For the Fortran code that calculates the non-interacting susceptibility χ_0, please, see Appendix D.3.

When a vector $\vec{k}+\vec{q}$ takes one part of the Fermi surface to another part of the Fermi surface, $\vec{q}$ is said to be a nesting vector. Thus, when the nesting vector exists, $E(k+q)-E(k)=0$ in the relation (3.10), and then with the accumulation of several nesting vectors, a peak in the non-interacting susceptibility is created.

The non-interacting susceptibility is the starting point for developing the MRPA method, which in turn considers Coulomb interactions, as will be shown in the next section.

3.2.3 Interacting Susceptibility - χ^{RPA}

Once we have the non-interacting susceptibility χ_0, Eq. (3.10), we can calculate the charge and spin susceptibilities, given by the Dyson equations (3.11) and (3.12), please see at Ref. (GRASER et al., 2009). Both charge and spin susceptibilities will measure the response of the system to a corresponding external perturbation.

$$(\chi^{RPA}_{\text{charge}})^{pq}_{st} = (\chi_0)^{pq}_{st} - (\chi^{RPA}_{\text{charge}})^{pq}_{uv}(U^c)^{uv}_{wz}(\chi_0)^{wz}_{st} \tag{3.11}$$

$$(\chi^{RPA}_{\text{spin}})^{pq}_{st} = (\chi_0)^{pq}_{st} + (\chi^{RPA}_{\text{spin}})^{pq}_{uv}(U^s)^{uv}_{wz}(\chi_0)^{wz}_{st} \tag{3.12}$$

Inverting the Dyson equation, we obtain the charge and spin susceptibilities, Eqs. (3.13) and (3.14), respectively.

$$\chi^{RPA}_{\text{charge}} = \chi_0(\mathbb{1}+U^c\chi_0)^{-1} \tag{3.13}$$

$$\chi^{RPA}_{\text{spin}} = \chi_0(\mathbb{1}-U^s\chi_0)^{-1} \tag{3.14}$$

If we take the diagonal of the interacting susceptibility tensor for the spin and charge cases, we obtain the relations (3.15) and (3.16), respectively.

$$\chi^{RPA}_{S}(\vec{q}) = \frac{1}{2}\sum_{sp}(\chi^{RPA}_{\text{spin}})^{pp}_{ss}(\vec{q},0) \tag{3.15}$$

$$\chi^{RPA}_{\text{c}}(\vec{q}) = \frac{1}{2}\sum_{sp}(\chi^{RPA}_{\text{charge}})^{pp}_{ss}(\vec{q},0) \tag{3.16}$$

The inclusion of Coulomb interactions in the susceptibilities is in Section 4.2.3, and the code for obtaining the interacting susceptibilities is in Appendix D.4. These susceptibilities have a fundamental role in the next section, where we will show how the pairing vertex (Γ) is calculated.

3.2.4 Pairing vertex - Γ

Considering that the pairing mechanism responsible for superconductivity is through spin and/or charge fluctuations, we can calculate the pairing vertex in the MRPA approximation, where we have, for the singlet case (GRASER et al., 2009),

$$\Gamma^{pq}_{st}(\vec{k},\vec{k}',\omega) = \Big[\frac{3}{2}U^S\chi^{RPA}_S(\vec{k}-\vec{k}',\omega)U^S + \frac{1}{2}U^S - \frac{1}{2}U^C\chi^{RPA}_{\text{c}}(\vec{k}-\vec{k}',\omega)U^C + \frac{1}{2}U^C\Big]^{tq}_{ps}. \tag{3.17}$$

For the triplet case (TAKIMOTO; HOTTA; UEDA, 2004), the $\Gamma_{st}^{pq}(\vec{k},\vec{k}',\omega)$ equation to be considered is given by

$$\Gamma_{st}^{pq}(\vec{k},\vec{k}',\omega) = \Big[-\frac{1}{2}U^S\chi_S^{RPA}(\vec{k}-\vec{k}',\omega)U^S + \frac{1}{2}U^S - \frac{1}{2}U^C\chi_c^{RPA}(\vec{k}-\vec{k}',\omega)U^C + \frac{1}{2}U^C\Big]_{ps}^{tq}. \quad (3.18)$$

Considering only the real part of the pairing interaction at $\omega = 0$, from the Kramers–Kronig relation, and considering that most the relevant effects occur at the Fermi surface, we can calculate the scattering from the pair-state $(\vec{k},-\vec{k})$ on the Fermi surface point k (labeled as i) to the pair-state $(\vec{k}',-\vec{k}')$ on the Fermi surface point k' (labeled as j),

$$\Gamma_{ij}(\vec{k},\vec{k}') = \sum_{stpq} a_{\nu i}^{t,*}(-\vec{k})a_{\nu i}^{s,*}(\vec{k})\mathrm{Re}[\Gamma_{st}^{pq}(\vec{k},\vec{k}',0)]a_{\nu j}^{p}(\vec{k}')a_{\nu j}^{q}(-\vec{k}'), \quad (3.19)$$

where Γ_{ij} is only the symmetric part of the pairing vertex

$$\frac{1}{2}[\Gamma_{ij}(\vec{k},\vec{k}') + \Gamma_{ij}(\vec{k},-\vec{k}')] \quad (3.20)$$

for the spin singlet subspace. We assume only the symmetric part to ensure that the resulting pairing wave function is consistent with the symmetry properties of the singlet states.

3.2.5 Eigenvalue equation - λ_α and g_α

Our goal is to find the pairing-functions, and their symmetries, that satisfy the following expression,

$$-\sum_j \oint_{C_j} \frac{d\vec{k}'_\parallel}{2\pi} \frac{1}{2\pi v_F(\vec{k}')}\Gamma_{ij}(\vec{k},\vec{k}')g_\alpha(\vec{k}') = \lambda_\alpha g_\alpha(\vec{k}), \quad (3.21)$$

where λ_α indicates the eigenvalues of the pairing vertex, with corresponding eigenvectors $g_\alpha(\vec{k})$ (gap-function).

We will break down the Eq.(3.21), to understand its components term by term. The first elements that stand out are the sum and the integral, where the sum computes the contribution of all the pockets on the Fermi surface, while the integral goes through each point on the Fermi surface, which has been previously discretized in to a set of points.

The Fermi velocity is defined by $v_F(\vec{k}) = |\nabla_{\vec{k}}E_\nu(\vec{k})|$ and the factor $(1/2\pi v_F(\vec{k}))$ is a normalization factor, while the pairing vertex represents the effective interaction between the pair-states $\vec{k}$ and $\vec{k}'$ in pockets i and j of the Fermi surface, respectively. This interaction function incorporates the contributions of the electronic interactions in the material.

The $g_\alpha(\vec{k})$ is the momentum-dependent pairing gap-function, which describes the paired state of the system in the pairing channel α, where λ_α is the eigenvalue associated with the pairing channel α. For more details on the calculation and the code used, see Appendix D.5.

3.2.6 Convergence Study

In computer simulations, one of the most fundamental steps during the production of results is to ensure that the input parameters provide converged data. In this context, for the

MRPA method, the best way to assess the convergence of the simulation is by checking if (and how) the symmetry of the leading gap function (eigenvector of the highest eigenvalue of the integrand in Eq. (3.21)) changes with the parameters of the simulation. The relevant parameters to test convergence are those that control the discretization of the BZ and the discretization of the Fermi surface.

Equation (3.21) gives us the eigenvalues and eigenvectors for a given value of U, for a given discretization of the Brillouin zone (for the calculation of χ_0), and a given discretization of the Fermi surface (to determine the dimension of the matrix to be diagonalized). To illustrate the convergence of the simulations, we evaluate the symmetry of the eigenvectors at doping $n = 4.35$, Fig 8, as we progressively improve the resolution of both discretizations.

The Brillouin zone is discretized in the interval $[-\pi, \pi)$ into N points, both on the k_x and k_y axes, and the non-interacting susceptibility χ_0 is calculated at those points. The points $q = k - k'$, where χ_0 must be calculated (to then calculate the pairing vertex), are not part of the points that form the grid in which the BZ was discretized. Thus, for each point $q = k - k'$, we take the four closest points in the Brillouin zone grid (where χ_0 has been calculated) and interpolate the value of χ_0 at q. With that, we can calculate the pairing vertex $\Gamma(\vec{k}, \vec{k}')$ that scatters a pair-state between points k and k' located at the Fermi surface.

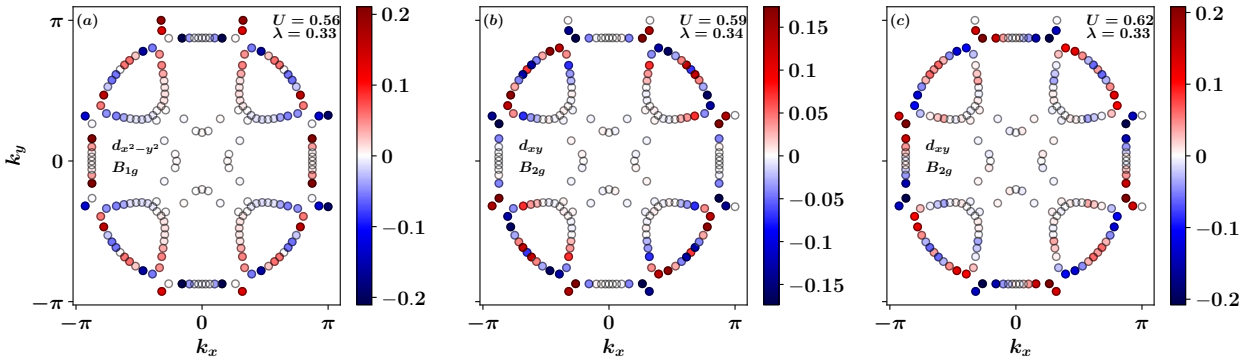

Figure 8 – Gap-function results for the leading eigenvalue of the pairing vertex, obtained from Eq. (3.21). The results from panel (a) to (c) are for BZ grids 32×32, 64×64, and 128×128, respectively, where N is the number of q_x (and q_y) values that discretize the BZ. Since the eigenvalues λ depend on U, we chose the U values (for each different N simulation) so that the leading eigenvalues are similar in all three cases. Note that the discretization of the Fermi surface is fixed at 196 points (indicated by circles). The color map indicates the value of the gap-function at each point on the Fermi surface. The gap-function symmetries are indicated. We see that from $N = 32$ to $N = 64$ there is a change from B_{1g} to B_{2g} (D_{4h} symmetry group), indicating that there was no convergence yet, which is achieved for $N = 128$.

It is expected that with a finer resolution in the BZ discretization (larger N values), the interpolation of the non-interacting susceptibility χ_0 should be more precise, and consequently the matrix elements of the pairing vertex Γ will be more precise, and thus its eigenvalues and eigenvectors should converge, with higher N values, to the correct superconducting state. As

shown by the legends indicating the symmetry of the gap-function in each panel, the $N = 32$ results had not converged yet. Convergence is obtained for $N = 128$. Obviously, increasing the discretization of the Brillouin zone implies a substantial increase in computational cost, so the calculations were only possible thanks to the use of the computing clusters ate CENAPAD-SP (CENAPAD-SP,), where the χ_0 simulation with a 128×128 grid took about 17 hours, with a total memory cost of 123 $G!B$ [2]

With the convergence of the BZ discretization (for 128×128), we can evaluate how the discretization of the Fermi surface affects the convergence of the symmetry of the pairing vertex $\Gamma(\vec{k}, \vec{k}')$, see Fig. 9.

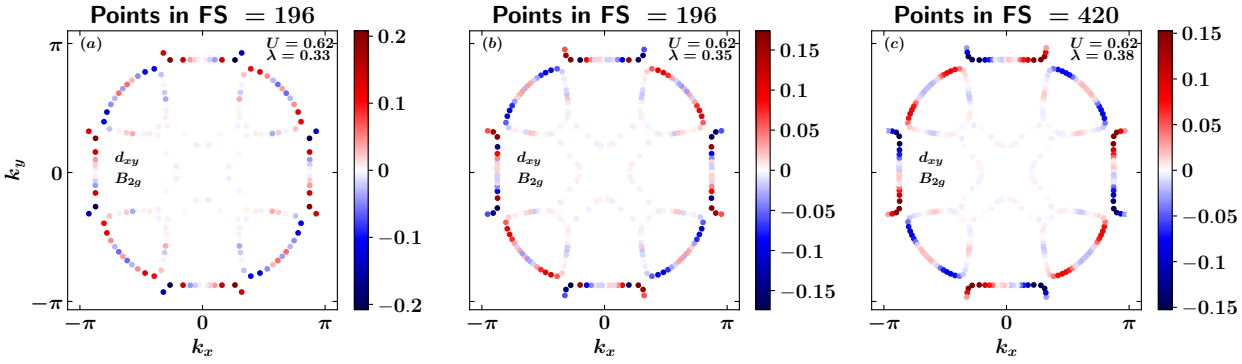

Figure 9 – Gap function for the leading eigenvalue for Eq. (3.21) for a given value of U, where the BZ discretization of is fixed at 128×128 points. In panels (a), (b) and (c), we have the FS discretizations with 196, 308, and 420 points, respectively. Notice

According to Fig. 9, the symmetry of the gap function was preserved with an increase in the number of points on the FS. However, taking in account a larger number of pair scattering events, at fixed $U = 0.62$, resulted in an increase of the leading eigenvalue, from 0.33 to 0.38 (an increase of almost 20%).

In order to ensure convergence of the gap-function, a final change was made to the BZ discretization, going from 128×128 points to 158×158 points, see Fig. 10.

In all the following simulations in this dissertation, the parameters used were as follows:

- Points in the Brillouin zone: 158×158;
- Points in the Fermi surface: 420;
- Temperature: 10^{-4}K
- Green's function imaginary part: 10^{-5}

[2] Notice that the calculation of χ_0 at a q point of the BZ requires a sum over all points in the BZ, please, see Eq. (3.10).

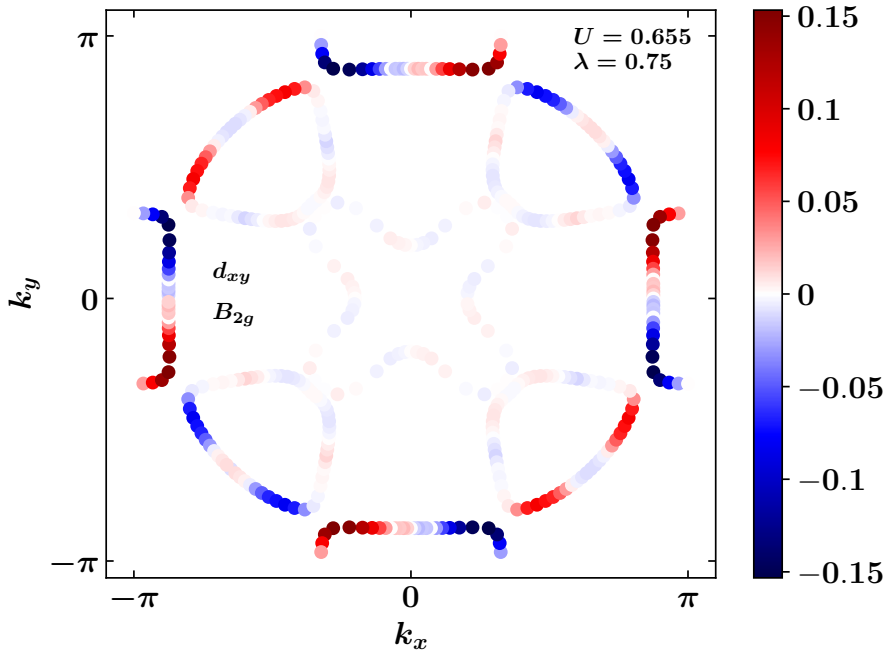

Figure 10 – Gap-function for the leading eigenvalue $\lambda = 0.75$, for 158×158 BZ discretization, and 420 points on the Fermi surface. The gap-function has d_{xy} symmetry and takes the largest amplitudes at the outer edges of the pockets.

4 Chromium Superconductors

Based on the concepts and predictions of BCS theory, we should also introduce the other classes of superconductors, the so-called unconventional superconductors (UcS). As a definition for UcS we will use the electron pairing mechanism, i.e., the attraction between the pairs and the formation of a superconducting state is due to other mechanisms that the BCS theory does not explain (STEWART, 2017) , for example spin fluctuation.

That definition creates a problem: the variety of materials with different pairing mechanisms between electron pairs. However, some characteristics are commonly found in this class of materials. The first characteristic is that most UcS have strong electronic correlations, differing in the atomic orbitals that are strongly interacting, for example, the organic superconductors have pairing dependent on the p-electrons (Jérome, D. et al., 1980; PARKIN et al., 1983), whereas the cuprates or iron superconductors have strongly correlated d-shell electrons (DAGOTTO, 1994; ORENSTEIN; MILLIS, 2000; KIM et al., 2021) or the heavy fermions are dependent on the f-shell (STEWART, 1984; VARMA, 2020).

The second common feature found in UcS is the instabilities in the materials, the main one being antiferromagnetism (STEWART, 2017; STEGLICH et al., 1979; DAGOTTO, 1994), but charge density waves (CDW) can also be found (AISHWARYA et al., 2023; VENDITTI; CAPRARA, 2023). Another property common to these compounds is their bidimensional behavior, which plays an important role in the formation of UcS. To illustrate this behavior, we will use cuprates. The resistivity in the ab-plane of the crystallographic axes can be 1000 times lower than the resistivity along the c-axis (STEWART, 2017).

Despite the identification of common properties in UcS, there is still no microscopic theory capable of describing the pairing mechanisms, as the BCS theory has done. Below, we will provide a historical overview of the subclasses of UcS.

4.1 Historic Perspective

In 1979, the first UcS was discovered, $CeCu_2Si_2$ ($T_c = 0.6K$) (STEGLICH et al., 1979), in which the superconducting phase coexists with local magnetic moments, which in turn, the BCS theory does not explain the materials superconductivity. The discovery of $CeCu_2Si_2$ began the search for new superconducting compounds with increasingly higher critical temperatures.

The $CeCu_2Si_2$ compound is classified as a heavy-fermion, where some heavy-fermions are unconventional superconductors. This name comes from the fact that conduction electrons can have an effective mass of over 1000 times the rest mass of the free electron. It was then discovered that the high effective mass of electrons plays a fundamental role in contributing to the resistivity of materials via electron-electron interaction.

Despite the new discovery, the scientific community's interest soon shifted to another class

of compounds, the so-called Cuprates, where some cuprates are unconventional superconductors. Cuprates are stacked materials that have planes of CuO_2 and other planes with ions, usually formed by the elements lanthanum, barium, strontium. The first cuprate discovered was BaLaCuO in 1986 (BEDNORZ; MÜLLER, 1986), at the time the highest critical temperature ever detected was $T_c = 23K$, while BaLaCuO has $T_c = 35K$. Throughout the remaining years of the 20th century, the scientific community searched for cuprates with increasingly higher T_c, reaching the point where the current record of $T_c = 138K$ was obtained for the compound $Hg_{12}Tl_3Ba_{30}Ca_{30}Cu_{45}O_{127}$ (CAO et al., 2021), at ambient pressure.

In addition to the high critical temperatures of cuprates, the superconductivity of this subclass is intrinsically associated with the doping of the materials, where it is possible to obtain two different dopings, one with electrons and one with holes. Both different dopings appear to have different pairing mechanisms, and therefore each will have different critical temperatures, with the hole doping having the highest critical temperature. Although the pairing mechanism of cuprates is not yet fully understood, the role that cuprates have played in the discovery of new UcS is of great importance, particularly in the discovery of iron superconductors.

In 2008, high critical temperature iron superconductors (KAMIHARA et al., 2008) were discovered, and similar to cuprates, the new materials have a plane with iron atoms, and above and below the plane are a variety of ions, such as N, P, As, Sb, Bi, called pnictides, or O, S, Se, Te, called chalcogenides. Where only the pnictides have 1111 systems formed by RFeAsO (R are rare earth elements).

Despite the variety of compounds, the vast majority are not described by the BCS theory, in which calculations for these materials the critical temperature is around $1K$, while experimentally $T_c \sim 50K$. Thus, the formation of the superconducting phase is associated with the Coulomb interaction between the electrons. However, it has been discovered that this interaction in iron superconductors is weaker than in cuprates, and therefore the theoretical treatment can be easier.

As with cuprates, the doping of iron superconductors is extremely important. In general, when the compounds are not doped, the materials exhibit a magnetic phase (spin density wave), predominantly antiferromagnetic. (DAGOTTO, 2013) Furthermore, doping with electrons or holes leads to three phases. The first is the Nematic phase, where a structural transformation takes place in which the elements align in a preferential direction but have no positional order. (STEWART, 2017)The second is the superconducting phase, and the third is the coexistence of these phases. However, the latter only occurs when doped with electrons.

The idea for explaining superconductivity in these materials is associated with the Coulomb interaction, but in principle only the electrons on the Fermi surfaces can take part in pair formation. Thus, spin fluctuations arise in order to increase the interactions between the electrons in the Fermi surface pockets, via the momentum $\vec{q}$ that connects the hole and electron pockets, which is the same as that which existed in the spin density wave state.

Research into iron-based high critical temperature superconductors began with the groundbreaking discovery of $26K$ superconductivity in LaFeAsO doped with F (KAMIHARA

et al., 2008). Since 2008, several other superconductors with a similar structure have been synthesized. All of these superconductors have FeAs or FeSe layers, widely considered to be the main component of these iron-based superconductors, just as CuO_2 layers are essential for high-T_c cuprates (DAGOTTO, 1994). The numerous similarities between iron-based superconductors and cuprates lie not only in the quasi-two-dimensional characteristics of the active layers, but also in the proximity of magnetically ordered states which, in various theoretical approaches, are considered responsible for inducing superconductivity through unconventional phonon-independent pairing mechanisms. However, at least in the case of As-based iron superconductors, the original magnetic compounds are metallic, unlike the Mott insulators found in cuprates, which establishes a significant difference between cuprates and pnictides.

Following the discovery of iron-based superconductivity, the search for superconducting phases with other transition metals began, in particular for Manganese and Chromium. In 2009, the first works with Manganese began to be published, $BaMn_2As_2$ is an isostructural compound to $BaFe_2As_2$, where at $T_N = 625K$ it is an antiferromagnetic insulator (SINGH; ELLERN; JOHNSTON, 2009; SINGH et al., 2009), and with hole doping the insulator-metal transition takes place causing a small reduction of T_N and of the ordered magnetic moment (SATYA et al., 2011). This suggests that the holes interact weakly with the Mn spins. However, no superconducting phase has yet been discovered for $BaMn_2As_2$. In the compound $LaMnAsO_{1-x}H_x$ (for $x \leq 0.73$) the substitution of oxygen for hydrogen results in the suppression of the antiferromagnetic order and the insulator-metal transition (HANNA et al., 2013), yet without the formation of a superconducting phase.

As for the Chromium compound, in 2013 LaCrAsO was synthesized with electron dopings (PARK et al., 2013), where the compound is a metal with a G-type magnetic structure, itinerant antiferromagnetism and a magnetic moment of $1.57\mu_B$, similar to iron superconductors. Also in the work done by Park *et al.* (PARK et al., 2013), the authors suggest that a superconducting phase should emerge, but it has not been observed. There are also theoretical studies that suggest that replacing Cr with Mn (electron doping) should lead to the emergence of a superconducting phase (PIZARRO et al., 2017; WANG et al., 2017). The study of the emergence of superconductivity in this material is the subject of this dissertation.

With the cuprates discovered in the 1980s, other isostructural compounds were theorized, one of them being the so-called Nickelates. However, in 2019 this compound $NdNiO_2$ was synthesized for the first time, and by replacing Nd with Sr (hole doping), a superconducting phase was found in thin films at $T_c \sim 15K$ (LI et al., 2019). Doping with Sr minimizes the self-doping effect, increases $p - d$ hybridization and produces Ni^2+ dopants with low spin ($S = 0$, non-magnetic). The crystal structure of infinite-layer nickelates $NdNiO_2$ is similar to that of cuprates, where superconductivity occurs in the NiO_2 planes, similarly to cuprates, where superconductivity emerges in the CuO_2 planes. However, there is still no consensus in the scientific community regarding the pairing mechanism of nickelates, but understanding the mechanism of nickelates may be the key to understanding the pairing mechanism of cuprates.

4.2 MRPA results

Using the five Cr $3d$ orbitals, the tight-binding model can satisfactorily represent the electronic states near the Fermi surface. The hopping integrals entering in the expressions for $T^{\mu\nu}(\mathbf{k})$ (see Eq. (4.1)) can be found in Ref. (WANG et al., 2017). They were obtained from a full DFT band structure calculation through a Wannierization procedure (WANG et al., 2017), as described for graphene in Chap. 3.

The independent electron Hamiltonian H_{TB} describing LaCrAsO (WANG et al., 2017) is given by

$$H_{\mathrm{TB}} = \sum_{\mathbf{k}\sigma\mu\nu} T^{\mu\nu}(\mathbf{k}) d^{\dagger}_{\mathbf{k}\mu\sigma} d_{\mathbf{k}\nu\sigma} \ , \tag{4.1}$$

where $d_{\mathbf{k}\nu\sigma}$ creates an electron with momentum $\mathbf{k}$, spin σ, in an orbital ν that is either t_{2g} (xy, zx, yz) or e_g ($3z^2 - r^2$) and ($x^2 - y^2$). In Fig. 11, the band structure and the density of states DOS are in panels (a) and (b), respectively.

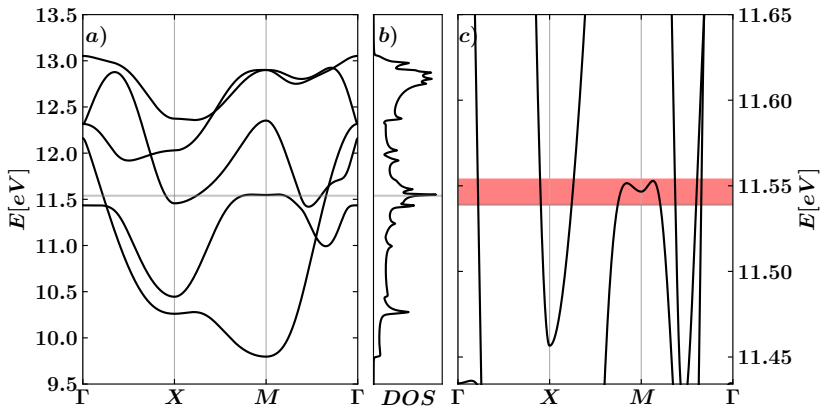

Figure 11 – (a) Band structures on the high symmetry lines on the $\Gamma - X - M - \Gamma$ path for the d orbitals of Cr. (b) Density of States (DOS) in the same energy range as panel (a). (c) Zoom in on the band structure to indicate the dopings (in red) analyzed in this work and their respective chemical potentials (μ), Table 4.2, which are important for the construction of Figure 13.

The total Hamiltonian $H_{\mathrm{T}} = H_{\mathrm{TB}} + H_{\mathrm{MB}}$ includes, besides H_{TB}, also the many-body term H_{MB} (KUBO, 2007):

$$\begin{aligned} H_{\mathrm{MB}} \ = \ & U \sum_{i,\mu} n_{i\mu\uparrow} n_{i\mu\downarrow} + U' \sum_{i,\mu<\nu} n_{i\mu} n_{i\nu} \\ & + J \sum_{i,\mu<\nu} \sum_{\sigma,\sigma'} d^{\dagger}_{i,\mu\sigma} d^{\dagger}_{i,\nu\sigma'} d_{i\mu\sigma'} d_{i\nu\sigma} \\ & + J' \sum_{i,\mu\neq\nu} d^{\dagger}_{i\mu\uparrow} d^{\dagger}_{i\mu\downarrow} d_{i\nu\downarrow} d_{i\nu\uparrow}, \end{aligned} \tag{4.2}$$

where μ, ν denote the Cr $3d$-orbitals, $n_{i,\nu}$ is the electron density of the orbital ν at a Chromium site i. We will use the usual relations $U' = U - 2J$, as well as $J = J'$, which are imposed by

symmetry (DAGOTTO; HOTTA; MOREO, 2001). Following standard procedure, we will fix the ratio $J/U = 0.25$ and vary U (MARTINS; MOREO; DAGOTTO, 2013). As mentioned in Chap. 3, increasing U may lead to a divergence in either the spin or charge susceptibility, which in turn leads to a divergence in the pairing vertex (see lower panel in Fig. 7), which may indicate a system instability towards superconductivity. Note that our energy unit is electron volt.

In 2013, Park, Sang-Won *et al.* succeeded for the first time in synthesizing stable compounds of LaCrAsO doped with electrons (PARK et al., 2013). This allowed them to investigate the electronic and magnetic structure of the compounds without and with doping (PIZARRO et al., 2017; WANG et al., 2017). Due to the Cr-O planes present in LaCrAsO compounds, such as appear in iron superconductors (KAMIHARA et al., 2008) and cuprates, the search for a superconducting phase in this new compound was initiated.

The first paper to suggest theoretical evidence of a possible superconducting phase was Pizzaro, J. M. *et at.* (PIZARRO et al., 2017), Fig. 12, where starting from the DFT calculation they carried out RPA with a modification of the band structure and found the d_{xy} symmetry of the gap function at $n = 4.5$ doping. After that, Wang, Wan-Sheng *et al.* performed a Functional Renormalization Group (FRG) calculation for different dopings of LaCrAsO (WANG et al., 2017). In the work of Wang, for dopings with holes the phase found was antiferromagnetic, while for some dopings with electrons the superconducting phase was found, whose gap function symmetry is $d_{x^2-y^2}$.

Based on previous work and using the codes discussed in Appendix B, we converged different chemical potentials, at their respective dopings, where there is a possibility of the superconducting phase being found for LaCrAsO. The dopings (n and n') and their respective chemical potentials (μ) for the tight-binding model described by the equation (4.1) are shown in Table 4.2.

n	n'	μ
4.35	0.35	11.539008998897742
4.36	0.36	11.540694083256154
4.37	0.37	11.542516834614567
4.38	0.38	11.544137834163733
4.39	0.39	11.545758426686644
4.40	0.40	11.547335178229595
4.41	0.41	11.548726897740130
4.42	0.42	11.550048458228074
4.43	0.43	11.551103369992505
4.44	0.44	11.552440161555978
4.45	0.45	11.553850062385736

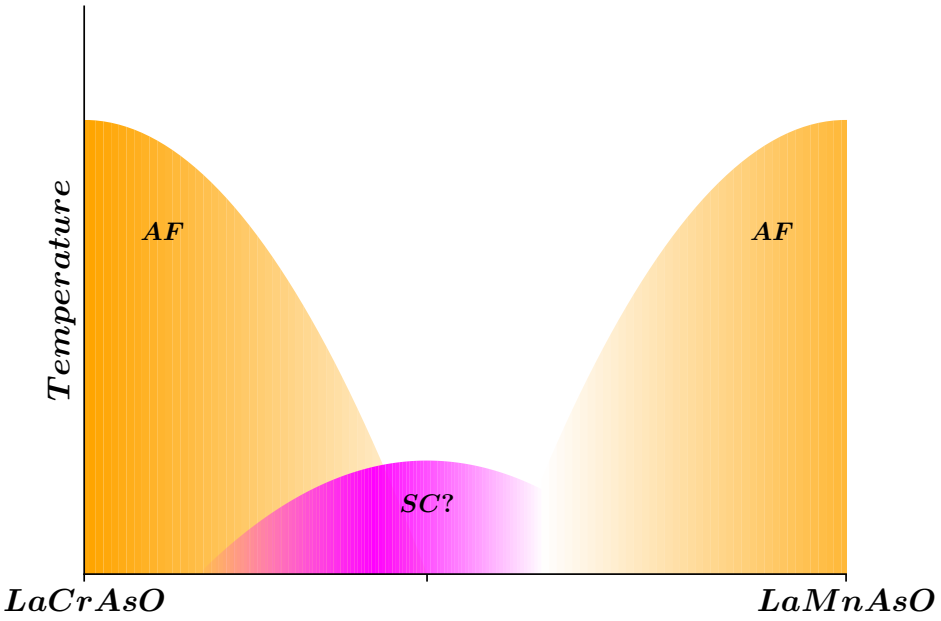

Figure 12 – Schematic of the simplified phase diagram for electron-doped LaCrAsO, where the Cr sites are replaced by Mn. For both low (PARK et al., 2013) and high (HANNA et al., 2013) doping, the system has an antiferromagnetic phase. For intermediate doping, it is possible that there is a superconducting phase (PIZARRO et al., 2017). Adapted from Ref. (PIZARRO et al., 2017).

4.2.1 Fermi Pockets

Using the values of the chemical potentials in Table 4.2, we diagonalized the Hamiltonian (4.1) in the entire Brillouin zone and obtained its eigenvalues $E(\vec{k})$. We show in Fig. 13 the Fermi surface for each doping in Table 4.2.

In Fig. 13 and 14, between the dopings $n = 4.42$ and $n = 4.43$ there is a change in the topology of the Fermi surface, called the Lifshitz transition. The Lifshitz transition is the change in the topology of the Fermi surface formed by the occupied quantum states of the material (LIFSHITZ et al., 1960; VOLOVIK, 2017), and this phenomenon can be associated with unconventional superconductivity, which coincides with the limit doping up to which an anomalous metallic phase (pseudo-gap) is observed in the vicinity of the superconducting phase and the doping characteristic of the Lifshitz transition. (BENHABIB et al., 2015; DOIRON-LEYRAUD et al., 2017). Additionally, this transition involves the emergence of points where the energy spectrum becomes zero within a system of many fermions, indicating that the conventional

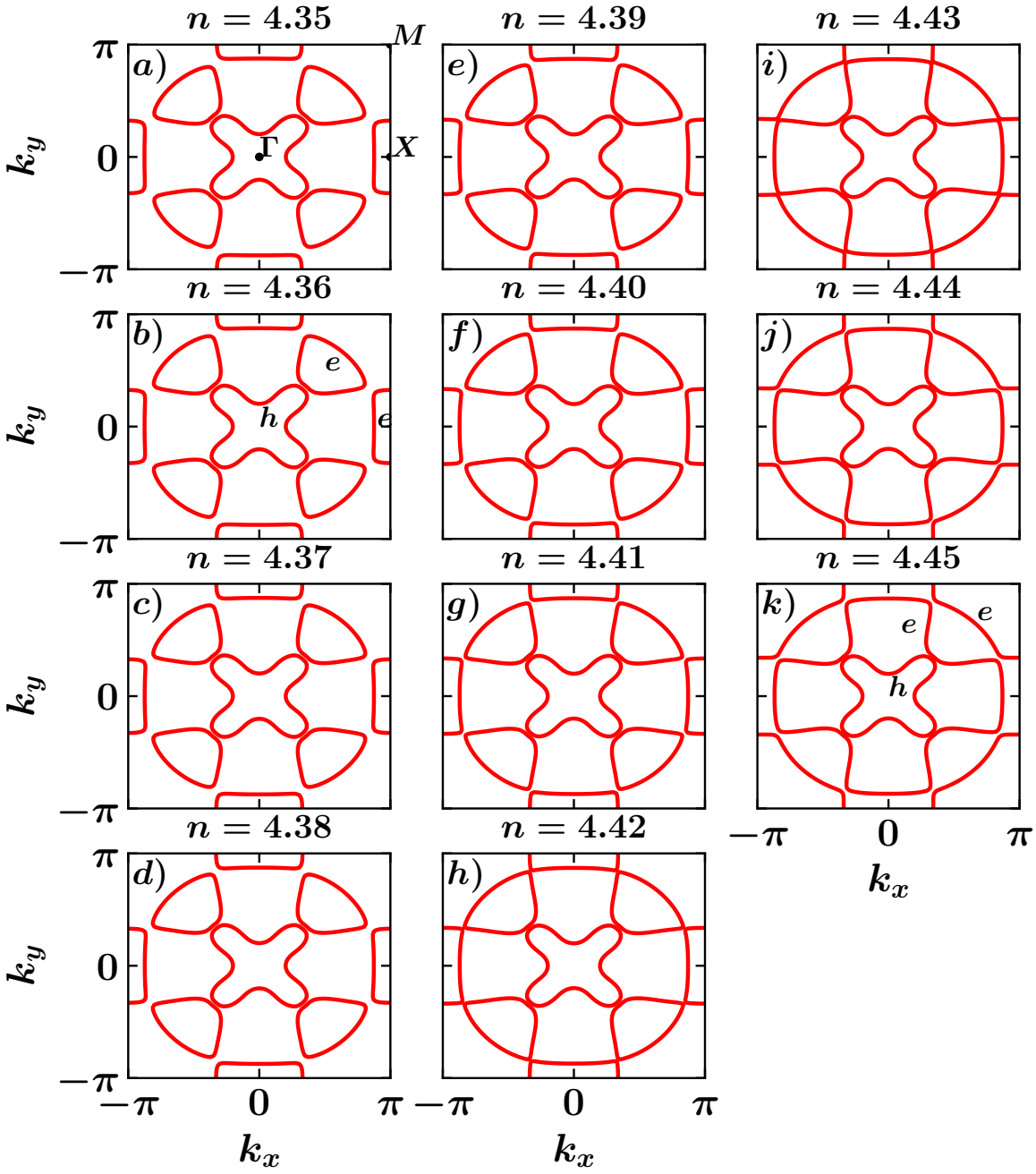

Figure 13 – Fermi surfaces in the Brillouin zone, with panels $a) - k)$ being the respective dopings $n = 4.35, 4.36, 4.37, 4.38, 4.39, 4.40, 4.41, 4.42, 4.43, 4.44, 4.45$. Note that a Lifshitz transition (LIFSHITZ et al., 1960) occurs between dopings $n = 4.42$ and $n = 4.43$, for more detail, please see Fig. 14.

Fermi surface is no longer part of this process. In more accessible terms, it is a quantum phase transition connected to shifts in the electronic structure of a material.

In condensed matter physics, such a transition can be noticed when there is a transfor-

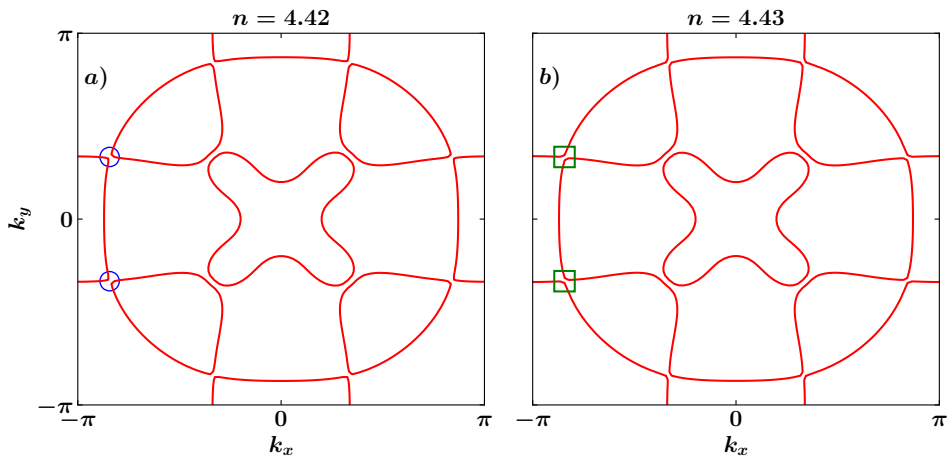

Figure 14 – Fermi surface in the Brillouin zone for dopings $n = 4.42$ and $n = 4.43$. Compared to the blue circles (panel (a)) and the green squares (panel (b)), the orientation of the Fermi surface curve has changed, i.e., the Lifshitz transition has occurred.

mation in the shape of the Fermi surface due to changes in external conditions, such as pressure or magnetic field. These changes can result in different electronic properties for the material, affecting its conductivity, for example.

For iron superconductors, on the other hand, when this Lifshitz transition occurs, the superconductivity in the M-centred electron pocket is slightly suppressed. In addition, a possible small superconducting gap with a dome-shaped doping dependence is observed in the new electron pocket at Γ (REN et al., 2017). And for LaCrAsO doping with electrons, superconducting instability appears close to the Lifshitz transition (PIZARRO et al., 2017).

4.2.2 Non-Interacting Susceptibility - χ_0

According to Section 3.2.6, we have established a standard for realizing RPA calculations. In this section, we will show the results of the non-interacting susceptibility (equation (3.10)), Fig. 15. We have selected three dopings of interest, two before and one after the Lifshitz transition, where the aim is to evaluate how the susceptibility is affected when the topology of the Fermi surface is modified.

About the results in Fig. 15, note that even after the Lifshitz transition, the non-interacting susceptibility does not change much, except that closer to the transition, there is a concentration of non-interacting susceptibility around the Γ point, please see Fig. 16. This may be an indication of a trend seen in Fig. 17, where the interacting susceptibility diverges at the Γ point.

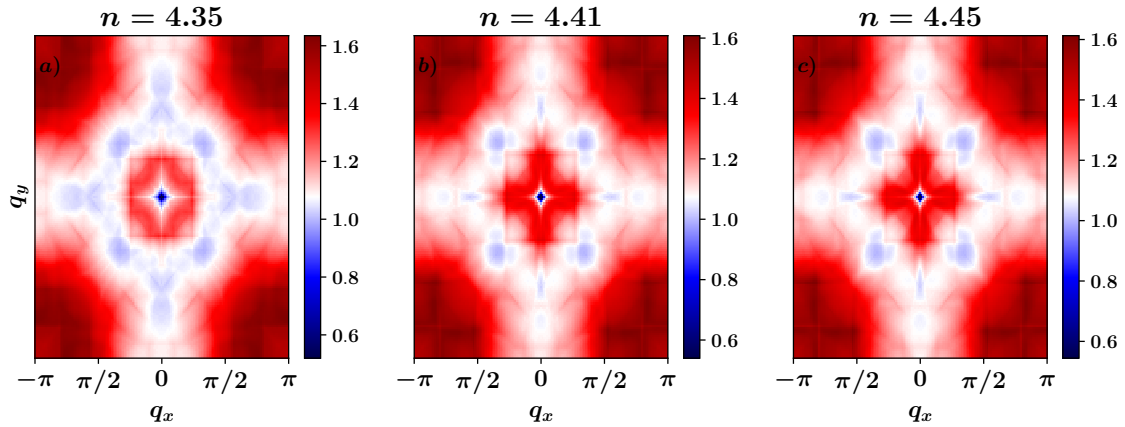

Figure 15 – Heat map of non-interacting susceptibility in the first Brillouin zone for the dopings $n = 4.35$, 4.41 and 4.45, in the panels a), b) and c), respectively. Note that the non-interacting susceptibility does not diverge, and its lowest value is located at the Γ point, while it assumes the highest values around the M point.

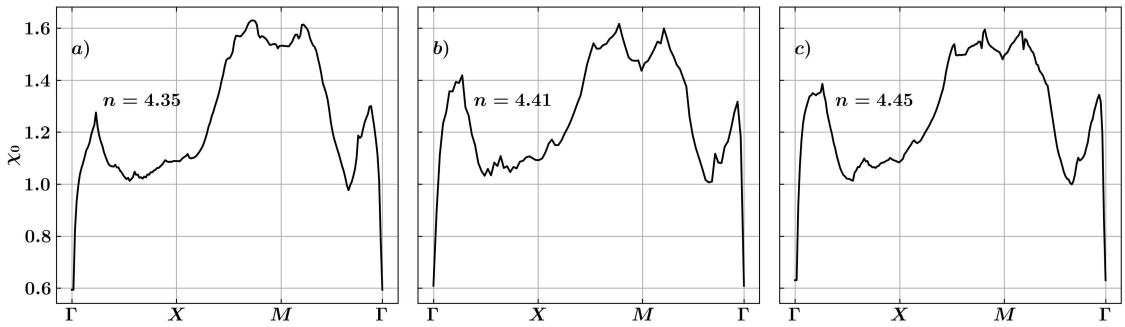

Figure 16 – Non-interacting susceptibility in the high symmetry lines $\Gamma - X - M - \Gamma$ for the dopings $n = 4.35$, 4.41 and 4.45, in the panels a), b) and c), respectively. At dopings $n = 4.41$ and $n = 4.45$ there was an increase in the peak around the Γ point, when compared to the $n = 4.35$ doping.

With the results of the non-interacting susceptibility in the three dopings of interest, in the next section we will introduce the electronic interactions and evaluate how they contribute to the properties of this system.

4.2.3 Interacting Susceptibility - χ^{RPA}

From the interaction Hamiltonian (4.2), we can show the non-zero matrix elements, according to Ref. (GRASER et al., 2009).

$$(U^c)^{aa}_{aa} = U; \quad (U^c)^{bb}_{aa} = 2U' - J; \quad (U^c)^{ab}_{ab} = -U' + 2J; \quad (U^c)^{ba}_{ab} = J'$$
$$(U^s)^{aa}_{aa} = U; \quad (U^s)^{bb}_{aa} = J; \quad (U^s)^{ab}_{ab} = -U'; \quad (U^s)^{ba}_{ab} = J'$$

Now, the Hamiltonian model that includes Coulomb interactions will be considered, and once we have it, we will evaluate how these interactions affect the interacting susceptibility (equations (3.15) and (3.16)), separating the contributions from the spins and the charges, Fig.

17. This separation is important to assess which fluctuation (spin or charge) is more probable to generate magnetic or superconducting instabilities, i.e., which interaction will be responsible for the 'glue' of the Cooper pairs.

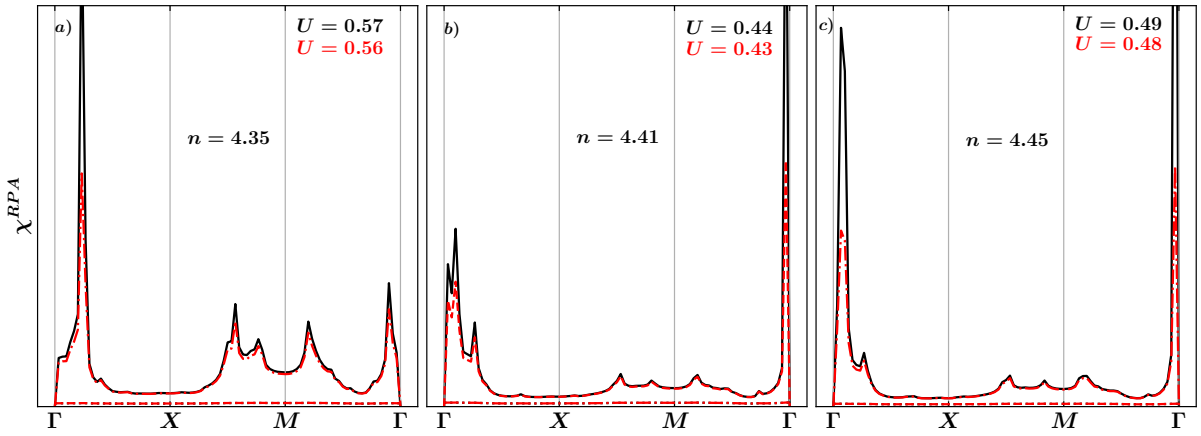

Figure 17 – Spin (solid and dash dotted lines) and charge (dashed and dotted lines) interacting susceptibility, with panels a), b) and c) being the respective dopings $n = 4.35, 4.41$ and 4.45. For each panel, we show the value of U that causes the spin susceptibility to diverge (black line) and the value of U before the divergence (red line).

Comparing the curves in Figure 17, when we evaluate the same dopings with the same U values, we see that the spin susceptibility contributions diverge, while the charge susceptibility do not.

In particular, when the U value increases, the charge susceptibility decreases, while the spin susceptibility increases. This behavior suggests that the system is affected more by spin fluctuations than charge fluctuations, i.e. the interaction that contributes most to the superconducting 'glue' (if the superconducting phase exists, please see section 4.2.4) will be the *spin fluctuation*.

The behavior of the interacting susceptibilities indicates that there are strong spin fluctuations, and these could be precursors of a magnetic order. In particular, the χ_S^{RPA} divergence near the Γ point suggests the formation of a ferromagnetic-type magnetic instability, see panel b) and c), in Fig. 17. While in panel a), in addition to the same magnetic instability, the spin susceptibility to order is also incommensurable, since the peak of the divergence is not at the point of symmetry.

In Ref. (BERK; SCHRIEFFER, 1966), the authors evaluated how magnetic ordering can affect the unconventional superconducting phase of a physical system. The authors concluded that antiferromagnetic ordering can influence the increase in critical temperature (T_c), as in cuprates, while ferromagnetism decreases the critical temperature. From this perspective, the

calculation of the spin susceptibility suggests that in the dopings studied for LaCrAsO, the critical temperature should be low, compared to cuprates, for example.

In the next section, we will show the calculation of the pairing vertex.

4.2.4 Pairing Vertex - Γ

In this section, we discuss the results of the pairing vertex and its diagonalization. We calculate λ_α as a function of the parameter U, for three different dopings. These results are presented in Fig. 18, for $n = 4.35$ 4.41, and 4.45, in panels (a) to (c), respectively. We show results for the 4 highest eigenvalues in each panel, presenting results for singlet pairing (solid curves).

In Fig. 19, we show the singlet pairing gap-function for the leading eigenvalue, for all three dopings, for values of U such that in all three panels the leading eigenvalue is in the range 0.9 ± 0.05, for the same dopings as in Fig. 18. An analysis of results indicates that the gap function symmetry remains constant, d_{xy} (B_{2g}), across the Lifshitz transition.

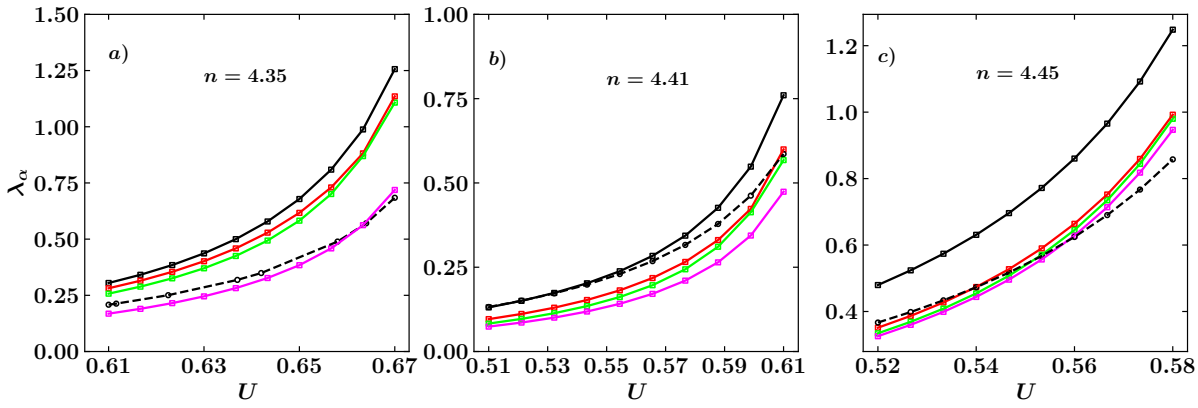

Figure 18 – Four highest singlet pairing eigenvalues λ_α as a function of U, at dopings $n = 4.35$, 4.41, and 4.45, in panels (a) to (c), respectively. The solid curves are for singlet pairing channels, while the dashed curves are for triplet pairing channels.

In Fig. 18, the behavior of the eigenvalues in relation to U is exponential, which is to be expected when compared to Ref. (GRASER et al., 2009). It is important to mention that the RPA method is valid for $0 \leq \lambda_\alpha \leq 1$. When $\lambda_\alpha = 0$, it indicates no pairing interactions for the given value of U. If $\lambda_\alpha = 1$, there is maximum pairing interaction, in which case the formation of a a superconducting state is possible. For $\lambda_\alpha > 1$, the RPA method presents convergence and instability problems, not allowing a valid physical interpretation of the results.

Also in Fig 18, we see that the curves for the triplet pairing have higher values of λ_α for the same values of U, compared to the singlet pairing channel. In Fig 17, the divergence in spin susceptibility indicates a tendency for the system to order ferromagnetically, while in Fig 18, the

singlet channels are prioritized over the triplet type, despite the fact that both compete with each other as the channel responsible for forming the superconducting state.

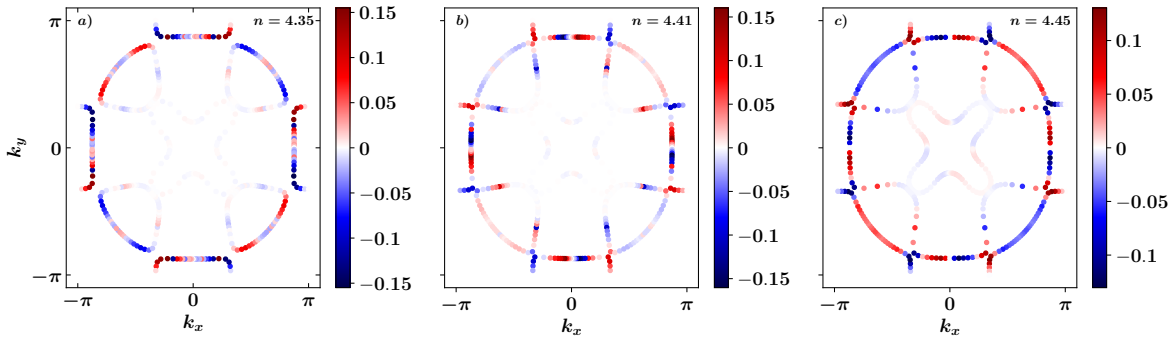

Figure 19 – The corresponding leading spin-singlet gap-function for the results in Fig. 18. We choose U values for each doping such that the leading eigenvalue is in the range 0.9 ± 0.05. The leading gap-function symmetry, d_{xy} (B_{2g}), is preserved across the Lifshitz transition.

In the work by Wang, Wan-Sheng, *et al.* (WANG et al., 2017), the authors performed functional Renormalization Group (fRG) calculations for $n = 4.35$, and find that the symmetry of the gap function is $d_{x^2-y^2}(B_{1g})$. However, in Fig. 19, $d_{xy}(B_{2g})$ symmetry was found for the same doping, in the singlet calculations. This difference is due to the different technique used in both works (MRPA vs. fRG).

The difference in symmetry, in relation to Ref. (WANG et al., 2017) can be explained when we analyze panel a) of Fig. 18, in which the first and second-highest eigenvalues (in the singlet pairing case) are close together. It is worth mentioning that the symmetry of the gap function for the second highest λ_α is $d_{x^2-y^2}(B_{1g})$. Therefore, there is competition between pairing channels of different symmetries, and each of the methods discussed, both in this dissertation and in the Ref. (WANG et al., 2017), prioritize certain pairing channels.

In Fig. 19, for the three dopings, the highest coefficients are concentrated at the edges of the outermost pockets in the Brillouin zone. This suggests that the pairing states are being influenced by the Lifshitz transition, since the concentration of states is present precisely in the pockets that have had their topology altered, see Fig. 13 for how the Lifshitz transition occurred.

This result may suggest that the Lifshitz transition, in addition to modifying the topology of the bands, in correlated systems can influence pairing mechanisms, in this case the superconducting mechanism via spin fluctuations.

Although the Lifshitz transition modifies the topology of the bands and can influence the pairing, it can be seen that the symmetry of the pairing channels did not change after the topological transition. In addition, the accumulation of g_α in some regions of the pockets may be indicative of the proximity of a Lifshitz transition.

5 Conclusions

In this work, we used the MRPA method to study the superconducting properties of LaCrAsO. The main motivation for that is to check if its doping-vs-temperature phase diagram presents magnetic and superconducting phases located nearby each other. This would make these Chromium superconductors similar to the cuprates and the iron pnictides. The main conclusions are as follows.

In Fig. 13 and Fig. 14, when changing the doping between $n = 4.35$ and $n = 4.45$, we verify that LaCrAsO has a Lifshitz transition between (approximately) $n = 4.42$ and $n = 4.43$. The gap function symmetry obtained, d_{xy} (B_{2g}), across the Lifshitz transition does not change. According to the results in Fig. 17, when including interactions, we can see that the charge susceptibility does not exert any influence on the system, contrary to the spin susceptibility, which tends to diverge, indicating a possible magnetic instability.

Furthermore, in Fig. 17, near the Lifshitz transition, the spin susceptibility suggests a ferromagnetic-type magnetic instability for all the dopings studied. At doping $n = 4.35$, there is some incommensurability (the divergence does not occur exactly at Γ). Despite a tendency for short-range ferromagnetic fluctuations, singlet pairing is dominant, although triplet pairing is not negligible.

Functional RG calculations (WANG et al., 2017) for the same doping as in Fig. 19(a), resulted in a different leading symmetry for singlet pairing, $d_{x^2-y^2}$, than the one obtained by us with MRPA, d_{xy}. This is not surprising, since both methods are widely different, and we found, using MRPA, that the sub-leading gap-function symmetry is $d_{x^2-y^2}$, with an eigenvalue close to the leading one [see Fig. 18(a) - the black curve corresponds to d_{xy} symmetry, while the red curve corresponds to $d_{x^2-y^2}$ symmetry].

With regard to the future prospects of this work, there are three approaches to be explored. Firstly, due to the high computational cost of carrying out the MRPA calculation, the implementation of a parallelized Fortran90 code would represent an advance in performance in terms of execution time, mainly for the χ_0 calculations, which are the most time and memory demanding.

The second is the technical side of the MRPA method. The calculation of the pairing vertex via MRPA is an intricate many-body problem, which results in the diagonalization of the Bethe-Salpeter kernel. A better understanding of how these equations are obtained would be an interesting project in itself as part of a PhD thesis.

In Fig. 11(a), around the BZ M point, there is a flat band and thus the density of states shows a peak. This peak in the density of states is called a Van Hove singularity. This singularity can be indicative of superconductivity with a higher critical temperature, as there is more available pairing between the electrons. However, this topic was not covered in this dissertation, and in the future this issue could be investigated in detail.

Bibliography

AISHWARYA, A. et al. Magnetic-field-sensitive charge density waves in the superconductor UTe_2. *Nature*, v. 618, p. 928, 2023. Disponível em: <https://doi.org/10.1038/s41586-023-06005-8>.

ANDERSON, P. The resonating valence bond state in La_2CuO_4 and superconductivity. *Science*, v. 235, p. 1196, 1987. Disponível em: <https://doi.org/10.1126/science.235.4793.1196>.

ASHCROFT, N. W.; MERMIN, N. D. *Solid state physics*. [S.l.]: Holt-Saunders, 1976.

BARDEEN, J.; COOPER, L. N.; SCHRIEFFER, J. R. Theory of superconductivity. *Phys. Rev.*, v. 108, p. 1175, 1957. Disponível em: <https://doi.org/10.1103/PhysRev.108.1175>.

BATLOGG, B.; VARMA, C. M. *The underdoped phase of cuprate superconductors – Physics World — physicsworld.com*. 2000. <https://physicsworld.com/a/the-underdoped-phase-of-cuprate-superconductors/>. [Accessed 18-06-2024].

BEDNORZ, J. G.; MÜLLER, K. A. Possible high T_c superconductivity in the BaLaCuO system. *Zeitschrift für Physik B Condensed Matter*, v. 64, p. 189, 1986. Disponível em: <https://doi.org/10.1007/BF01303701>.

BENHABIB, S. et al. Collapse of the normal-state pseudogap at a lifshitz transition in the $bi_2sr_2cacu_2o_{8+\delta}$ cuprate superconductor. *Phys. Rev. Lett.*, v. 114, p. 147001, 2015. Disponível em: <https://link.aps.org/doi/10.1103/PhysRevLett.114.147001>.

BERK, N. F.; SCHRIEFFER, J. R. Effect of ferromagnetic spin correlations on superconductivity. *Phys. Rev. Lett.*, v. 17, p. 433, 1966. Disponível em: <https://doi.org/10.1103/PhysRevLett.17.433>.

BERMON, S.; GINSBERG, D. M. Electron tunneling into superconducting mercury films. *Phys. Rev.*, v. 135, p. A306, 1964. Disponível em: <https://doi.org/10.1103/PhysRev.135.A306>.

BICKERS, N.; SCALAPINO, D. Conserving approximations for strongly fluctuating electron systems. I. Formalism and calculational approach. *Ann. Physics*, v. 193, p. 206, 1989. Disponível em: <https://www.sciencedirect.com/science/article/pii/000349168990359X>.

BICKERS, N. E.; SCALAPINO, D. J.; WHITE, S. R. Conserving approximations for strongly correlated electron systems: Bethe-Salpeter equation and dynamics for the two-dimensional Hubbard model. *Phys. Rev. Lett.*, v. 62, p. 961, 1989. Disponível em: <https://doi.org/10.1103/PhysRevLett.62.961>.

Buongiorno Nardelli, M. et al. PAOFLOW: A utility to construct and operate on ab initio Hamiltonians from the projections of electronic wavefunctions on atomic orbital bases, including characterization of topological materials. *Comput. Mater. Sci.*, v. 143, p. 462, 2018. Disponível em: <https://www.sciencedirect.com/science/article/pii/S0927025617306651>.

BÜSSER, C. A.; MARTINS, G. B.; FEIGUIN, A. E. Lanczos transformation for quantum impurity problems in d-dimensional lattices: Application to graphene nanoribbons. *Phys. Rev. B*, v. 88, p. 245113, 2013. Disponível em: <https://link.aps.org/doi/10.1103/PhysRevB.88.245113>.

CAO, Q. et al. Emerging field of few-layered intercalated 2d materials. *Nanoscale Adv.*, v. 3, p. 963, 2021. Disponível em: <https://doi.org/10.1039/D0NA00987C>.

CENAPAD-SP. *CENAPAD-SP*. <https://www.cenapad.unicamp.br/>. Accessed: 2024-05-23.

CERASOLI, F. T. et al. Advanced modeling of materials with PAOFLOW 2.0: New features and software design. *Comput. Mater. Sci.*, v. 200, p. 110828, 2021. Disponível em: <https://www.sciencedirect.com/science/article/pii/S0927025621005486>.

COOPER, L. N. Bound electron pairs in a degenerate Fermi gas. *Phys. Rev.*, v. 104, p. 1189, 1956. Disponível em: <https://doi.org/10.1103/PhysRev.104.1189>.

DAGOTTO, E. Correlated electrons in high-temperature superconductors. *Rev. Mod. Phys.*, v. 66, p. 763, 1994. Disponível em: <https://doi.org/10.1103/RevModPhys.66.763>.

DAGOTTO, E. Colloquium: The unexpected properties of alkali metal iron selenide superconductors. *Rev. Mod. Phys.*, v. 85, p. 849, 2013. Disponível em: <https://doi.org/10.1103/RevModPhys.85.849>.

DAGOTTO, E.; HOTTA, T.; MOREO, A. Colossal magnetoresistant materials: the key role of phase separation. *Phys. Rep.*, v. 344, p. 1, 2001. Disponível em: <https://www.sciencedirect.com/science/article/pii/S0370157300001216>.

DAI, P.; HU, J.; DAGOTTO, E. Magnetism and its microscopic origin in iron-based high-temperature superconductors. *Nat. Phys.*, v. 8, p. 709, 2012. Disponível em: <https://doi.org/10.1038/NPHYS2438>.

DOIRON-LEYRAUD, N. et al. Pseudogap phase of cuprate superconductors confined by Fermi surface topology. *Nat. Commun.*, v. 8, p. 2044, 2017. Disponível em: <https://doi.org/10.1038/s41467-017-02122-x>.

ENGEL, E.; DREIZLER, R. *Density Functional Theory: An Advanced Course*. Springer Berlin Heidelberg, 2011. ISBN 9783642140907. Disponível em: <https://books.google.com.br/books?id=R2_RBzVu3TUC>.

FAY, D.; LAYZER, A. Superfluidity of low-density fermion systems. *Phys. Rev. Lett.*, v. 20, p. 187, 1968. Disponível em: <https://doi.org/10.1103/PhysRevLett.20.187>.

GIAEVER, I.; HART, H. R.; MEGERLE, K. Tunneling into superconductors at temperatures below 1°K. *Phys. Rev.*, v. 126, p. 941, 1962. Disponível em: <https://doi.org/10.1103/PhysRev.126.941>.

GIANNOZZI, P. et al. Advanced capabilities for materials modelling with QUANTUM ESPRESSO. *J. Phys. Condens. Matter*, v. 29, p. 465901, 2017. Disponível em: <http://stacks.iop.org/0953-8984/29/i=46/a=465901>.

GIANNOZZI, P. et al. Quantum espresso: a modular and open-source software project for quantum simulations of materials. *J. Phys. Condens. Matter*, v. 21, p. 395502, 2009. Disponível em: <http://www.quantum-espresso.org>.

GRASER, S. et al. Near-degeneracy of several pairing channels in multiorbital models for the Fe pnictides. *New J. Phys.*, v. 11, p. 025016, 2009. Disponível em: <https://dx.doi.org/10.1088/1367-2630/11/2/025016>.

HANNA, T. et al. From antiferromagnetic insulator to ferromagnetic metal: Effects of hydrogen substitution in LaMnAsO. *Phys. Rev. B*, v. 87, p. 020401, 2013. Disponível em: <https://link.aps.org/doi/10.1103/PhysRevB.87.020401>.

HIRSCH, J.; MAPLE, M.; MARSIGLIO, F. Superconducting materials classes: Introduction and overview. *Phys. C Supercond. its Appl.*, v. 514, p. 1, 2015. Disponível em: <https://doi.org/10.1016/j.physc.2015.03.002>.

HUBBARD, J. Electrons correlations in narrow energy bands. *Proc. R. Soc. Lond.*, v. 276, p. 238, 1963. Disponível em: <https://doi.org/10.1098/rspa.1963.0204>.

HüFNER, S. *Photoelectron Spectroscopy*. Springer Berlin Heidelberg, 2003. ISSN 1439-2674. ISBN 9783662092804. Disponível em: <http://dx.doi.org/10.1007/978-3-662-09280-4>.

Jérome, D. et al. Superconductivity in a synthetic organic conductor (TMTSF)2PF 6. *J. Physique Lett.*, v. 41, n. 4, p. 95, 1980. Disponível em: <https://doi.org/10.1051/jphyslet:0198000410409500>.

KAMIHARA, Y. et al. Iron-based layered superconductor la[o1-xfx]feas (x = 0.050.12) with tc = 26 k. *J. Am. Chem. Soc.*, v. 130, p. 3296, 2008. Disponível em: <https://doi.org/10.1021/ja800073m>.

KIM, J. et al. Superconducting Sr2RuO4 thin films without out-of-phase boundaries by higher-order Ruddlesden–Popper intergrowth. *Nano Lett.*, v. 21, p. 4185, 2021. Doi: 10.1021. Disponível em: <https://doi.org/10.1021/acs.nanolett.0c04963>.

KOHN, W.; LUTTINGER, J. M. New mechanism for superconductivity. *Phys. Rev. Lett.*, v. 15, p. 524, 1965. Disponível em: <https://doi.org/10.1103/PhysRevLett.15.524>.

KOHN, W.; SHAM, L. J. Self-Consistent Equations Including Exchange and Correlation Effects. *Phys. Rev.*, v. 140, p. A1133, 1965. Disponível em: <https://link.aps.org/doi/10.1103/PhysRev.140.A1133>.

KORTUS, J. Current progress in the theoretical understanding of MgB₂. *Phys. C Supercond.*, v. 456, p. 54, 2007. Disponível em: <https://doi.org/10.1016/j.physc.2007.01.023>.

KUBO, K. Pairing symmetry in a two-orbital Hubbard model on a square lattice. *Phys. Rev. B*, v. 75, p. 224509, 2007. Disponível em: <https://link.aps.org/doi/10.1103/PhysRevB.75.224509>.

LAYZER, A.; FAY, D. Spin fluctuation exchange - mechanism for a superfluid transition in liquid-He-3. *Solid State Commun.*, v. 15, p. 599, 1974. Disponível em: <https://doi.org/10.1016/0038-1098(74)91152-1>.

LI, D. et al. Superconductivity in an infinite-layer nickelate. *Nature*, v. 572, n. 7771, p. 624, 2019. Disponível em: <https://doi.org/10.1038/s41586-019-1496-5>.

LIFSHITZ, I. et al. Anomalies of electron characteristics of a metal in the high pressure region. *Sov. Phys. JETP*, v. 11, n. 5, p. 1130, 1960.

LINDHARD, J. On the properties of a gas of charged paraticles. Vol: 28, 1954. Disponível em: <https://www.osti.gov/biblio/4405425>.

LONG, M. W. The phase diagram of the Hubbard model. *Int. J. Mod. Phys. B*, v. 05, p. 865, 1991. Disponível em: <https://doi.org/10.1142/S0217979291000468>.

MAITI, S.; CHUBUKOV, A. V. Superconductivity from repulsive interaction. *AIP Conf. Proc.*, v. 1550, n. 1, p. 3, 2013. Disponível em: <https://doi.org/10.1063/1.4818400>.

MALIK, G. *Superconductivity: A New Approach Based On The Bethe-Salpeter Equation In The Mean-field Approximation*. World Scientific Publishing Company, 2016. (Series On Directions In Condensed Matter Physics). ISBN 9789814733090. Disponível em: <https://books.google.com.br/books?id=bGDFCwAAQBAJ>.

MANGIN, P.; KAHN, R. *Superconductivity*. 1. ed. Basel, Switzerland: Springer International Publishing, 2016.

MARSIGLIO, F. Eliashberg theory: A short review. *Ann. Physics*, v. 417, p. 168102, 2020. Eliashberg theory at 60: Strong-coupling superconductivity and beyond. Disponível em: <https://doi.org/10.1016/j.aop.2020.168102>.

MARTINS, G. B.; MOREO, A.; DAGOTTO, E. RPA analysis of a two-orbital model for the BiS_2-based superconductors. *Phys. Rev. B*, v. 87, p. 081102, 2013. Disponível em: <https://link.aps.org/doi/10.1103/PhysRevB.87.081102>.

MATTHIAS, B. T.; GEBALLE, T. H.; COMPTON, V. B. Superconductivity. *Rev. Mod. Phys.*, v. 35, p. 1, 1963. Disponível em: <https://doi.org/10.1103/RevModPhys.35.1>.

MORIYA, T.; UEDA, K. Spin fluctuations and high temperature superconductivity. *Adv. Phys.*, v. 49, p. 555, 2000. Disponível em: <https://doi.org/10.1080/000187300412248>.

MOSTOFI, A. A. et al. An updated version of wannier90: A tool for obtaining maximally-localised Wannier functions. *Comput. Phys. Commun.*, v. 185, n. 8, p. 2309, 2014. Disponível em: <https://www.sciencedirect.com/science/article/pii/S001046551400157X>.

NAGAMATSU, J. et al. Superconductivity at 39 K in magnesium diboride. *Nature*, v. 410, n. 6824, 2001. Disponível em: <https://doi.org/10.1038/35065039>.

ONNES, H. K. The resistance of pure mercury at helium temperatures. *Leiden Comm.*, v. 1206, p. 1226, 1911.

ORENSTEIN, J.; MILLIS, A. J. Advances in the physics of high-temperature superconductivity. *Science*, v. 288, p. 468, 2000. Disponível em: <https://www.science.org/doi/abs/10.1126/science.288.5465.468>.

PARK, S.-W. et al. Magnetic structure and electromagnetic properties of LnCrAsO with a ZrCuSiAs-type structure (Ln = La, Ce, Pr, and Nd). *Inorg. Chem.*, v. 52, p. 13363, 2013. Disponível em: <https://doi.org/10.1021/ic401487q>.

PARKIN, S. S. P. et al. Superconductivity in a new family of organic conductors. *Phys. Rev. Lett.*, v. 50, p. 270, 1983. Disponível em: <https://link.aps.org/doi/10.1103/PhysRevLett.50.270>.

PICKETT, W. E. The dawn of the nickel age of superconductivity. *Nat. Rev. Phys.*, v. 3, p. 7, 2021.

PIZARRO, J. M. et al. Strong correlations and the search for high-T_c superconductivity in chromium pnictides and chalcogenides. *Phys. Rev. B*, v. 95, p. 075115, 2017. Disponível em: <https://link.aps.org/doi/10.1103/PhysRevB.95.075115>.

REN, M. et al. Superconductivity across lifshitz transition and anomalous insulating state in surface k–dosed (li_{0.8}fe_{0.2}oh)fese. *Sci. Adv.*, v. 3, n. 7, p. e1603238, 2017. Disponível em: <https://www.science.org/doi/abs/10.1126/sciadv.1603238>.

SATYA, A. T. et al. Pressure-induced metallization of $BaMn_2As_2$. *Phys. Rev. B*, v. 84, p. 180515, 2011. Disponível em: <http://link.aps.org/doi/10.1103/PhysRevB.84.180515>.

SCALAPINO, D. Superconductivity and spin fluctuations. *J. Low Temp. Phys.*, v. 117, p. 179, 1999. Disponível em: <https://link.springer.com/article/10.1023/A:1022559920049#citeas>.

SCALAPINO, D. J. The case for $d_{x^2y^2}$ pairing in the cuprate superconductors. *Phys. Rep.*, v. 250, p. 329, 1995. Disponível em: <https://api.semanticscholar.org/CorpusID:43967680>.

SCALAPINO, D. J. A common thread: The pairing interaction for unconventional superconductors. *Rev. Mod. Phys.*, v. 84, p. 1383, 2012. Disponível em: <https://doi.org/10.1103/RevModPhys.84.1383>.

SCHILLING, A. et al. Superconductivity above 130-K in the Hg-Ba-Ca-Cu-O system. *Nature*, v. 363, p. 56, 1993. Disponível em: <https://doi.org/10.1038/363056a0>.

SHY, Y. M.; TOTH, L. E.; SOMASUNDARAM, R. Superconducting properties, electrical resistivities, and structure of NbN thin films. *J. Appl. Phys.*, v. 44, p. 5539, 1973. Disponível em: <https://doi.org/10.1063/1.1662193>.

SINGH, Y.; ELLERN, A.; JOHNSTON, D. C. Magnetic, transport, and thermal properties of single crystals of the layered arsenide $BaMn_2As_2$. *Phys. Rev. B*, v. 79, p. 094519, 2009. Disponível em: <http://link.aps.org/doi/10.1103/PhysRevB.79.094519>.

SINGH, Y. et al. Magnetic order in $BaMn_2As_2$ from neutron diffraction measurements. *Phys. Rev. B*, v. 80, p. 100403, 2009. Disponível em: <http://link.aps.org/doi/10.1103/PhysRevB.80.100403>.

STEGLICH, F. et al. Superconductivity in the presence of strong Pauli paramagnetism: $CeCu_2Si_2$. *Phys. Rev. Lett.*, v. 43, p. 1892, 1979. Disponível em: <https://link.aps.org/doi/10.1103/PhysRevLett.43.1892>.

STEWART, G. R. Heavy-fermion systems. *Rev. Mod. Phys.*, v. 56, p. 755, 1984. Disponível em: <https://link.aps.org/doi/10.1103/RevModPhys.56.755>.

STEWART, G. R. Unconventional superconductivity. *Adv. Phys.*, Taylor & Francis, v. 66, p. 75, 2017. Disponível em: <https://doi.org/10.1080/00018732.2017.1331615>.

TAKIMOTO, T.; HOTTA, T.; UEDA, K. Strong-coupling theory of superconductivity in a degenerate Hubbard model. *Phys. Rev. B*, v. 69, p. 104504, 2004. Disponível em: <https://doi.org/10.1103/PhysRevB.69.104504>.

VARMA, C. M. Colloquium: Linear in temperature resistivity and associated mysteries including high temperature superconductivity. *Rev. Mod. Phys.*, v. 92, p. 031001, 2020. Disponível em: <https://link.aps.org/doi/10.1103/RevModPhys.92.031001>.

VENDITTI, G.; CAPRARA, S. Charge-density waves vs. superconductivity: Some results and future perspectives. *Condensed Matter*, v. 8, n. 3, 2023. Disponível em: <https://doi.org/10.3390/condmat8030054>.

VERMA, P.; TRUHLAR, D. G. Status and challenges of density functional theory. *Trends Chem.*, v. 2, p. 302, 2020. Disponível em: <https://www.sciencedirect.com/science/article/pii/S2589597420300411>.

VOLOVIK, G. E. Topological Lifshitz transitions. *Low Temp. Phys.*, v. 43, p. 47, 2017. Disponível em: <https://doi.org/10.1063/1.4974185>.

WANG, L. et al. Paramagnons and high-temperature superconductivity in a model family of cuprates. *Nat. Commun.*, v. 13, 2022. Disponível em: <https://doi.org/10.1038/s41467-022-30918-z>.

WANG, W.-S. et al. Possible superconductivity in the electron-doped chromium pnictide LaOCrAs. *Phys. Rev. B*, v. 95, p. 144507, 2017. Disponível em: <https://doi.org/10.1103/PhysRevB.95.144507>.

WEBB, G. W. Low-temperature electrical resistivity of pure niobium. *Phys. Rev.*, v. 181, 1969. Disponível em: <https://link.aps.org/doi/10.1103/PhysRev.181.1127>.

WHITE, S. R. Density matrix formulation for quantum renormalization groups. *Phys. Rev. Lett.*, v. 69, p. 2863, 1992. Disponível em: <https://link.aps.org/doi/10.1103/PhysRevLett.69.2863>.

Appendix

APPENDIX A – Second Quantization

Consider a N-site crystal lattice, where the sites are labelled as $\vec{r}_i$ where $i = 1, \cdots, N$), where each quantum state is represented in terms of electron occupation at each site, viz., $|n_1, \cdots, n_N\rangle$. Creation and annihilation of electrons, with spin σ, on the i-th site are given by the operators

$$c^\dagger_{i,\sigma}|n_{1\sigma}, \cdots, n_{i\sigma}, \cdots, n_{N\sigma}\rangle = \sqrt{n_{i\sigma}+1}|n_{1\sigma}, \cdots, n_{i\sigma}+1, \cdots, n_{N\sigma}\rangle, \tag{A.1}$$

$$c_{i,\sigma}|n_{1\sigma}, \cdots, n_{i\sigma}, \cdots, n_{N\sigma}\rangle = \sqrt{n_{i\sigma}}|n_{1\sigma}, \cdots, n_{i\sigma}-1, \cdots, n_{N\sigma}\rangle, \tag{A.2}$$

which obey the anticommutation relations

$$\begin{aligned} \{c_{i\sigma}, c^\dagger_{j\sigma'}\} &= \delta_{ij}\delta_{\sigma\sigma'}, \\ \{c_{i\sigma}, c_{j\sigma'}\} &= \{c^\dagger_{i\sigma}, c^\dagger_{j\sigma'}\} = 0. \end{aligned}$$

In momentum space, the operators create or annihilate particles with momentum $\vec{k}$, so that

$$c^\dagger_{\vec{k}\sigma}|0\rangle = |\vec{k}, \sigma\rangle, \tag{A.3}$$

$$c_{\vec{k}\sigma}|\vec{k}, \sigma\rangle = |0\rangle, \tag{A.4}$$

where $|0\rangle$ is the vacuum state. Using the closure relation $\sum_\alpha |\alpha\rangle\langle\alpha| = \mathbb{1}$, we can change the basis, where the creation and annihilation operators in momentum space can be written in terms of the operators in position space, given by

$$c^\dagger_{\vec{k}\sigma} = \frac{1}{N}\sum_j e^{i\vec{k}\cdot\vec{r}_j} c^\dagger_{j\sigma} \tag{A.5}$$

$$c_{\vec{k}\sigma} = \frac{1}{N}\sum_j e^{-i\vec{k}\cdot\vec{r}_j} c_{j\sigma} \tag{A.6}$$

$$\tag{A.7}$$

and by using the Fourier transform, we can write the creation and annihilation operators in terms of the operators in reciprocal space.

APPENDIX B – Solution of the Hubbard model via the Hartree-Fock approximation

Before starting to study superconductivity, a study was carried out on the Hubbard model (B.1) and one of its possible ways of obtaining the model's solution, the Hartree-Fock method.

$$H = -t\sum_{ij\sigma} c^{\dagger}_{i\sigma}c_{j\sigma} + U\sum_{i} n_{i\uparrow}n_{i\downarrow} \tag{B.1}$$

Where t is the hopping term between sites in the unit cell, $c^{\dagger}_{i\sigma}$ ($c_{i\sigma}$) are creation (annihilation) operators, and U is the Hubbard term responsible for the interaction between electrons in the same site, and $n_{i\sigma}$ is the number operator.

The Hartree-Fock method is a self-consistent calculation (please see Section B.2) for evaluating the occupation of up and down spins at each site in the unit cell. So we built a code capable of determining the magnetic phases of a square lattice with two base sites, depending on the value of the Hubbard term U and the number of electrons in the system n_e, i.e. depending on the doping of the material.

The code produced can be summarized by the schematic diagram in Figure.20, where the difference between the initial and final electron occupancies at each site is always evaluated to determine the convergence of the self-consistent calculation.

From the self-consistent calculation, we were able to produce a magnetic phase diagram for the square lattice with two base sites, as shown in Figure 21 [1]. Note that the magnetic phase diagram respects the particle-hole symmetry that the Hamiltonian has. In addition, it can be seen that at zero doping, i.e. one electron per site, the system exhibits an antiferromagnetic phase regardless of the value of U.

B.1 Chemical Potential - μ

In addition to learning about systems with electron interactions, the Hubbard model code was fundamental for calculating the chemical potential used in the RPA code, in which the same logic for calculating the chemical potential for the Hubbard model was used in the RPA

[1] The results of this project were presented at the Autumn Meeting of the Brazilian Physics Society in 2023.

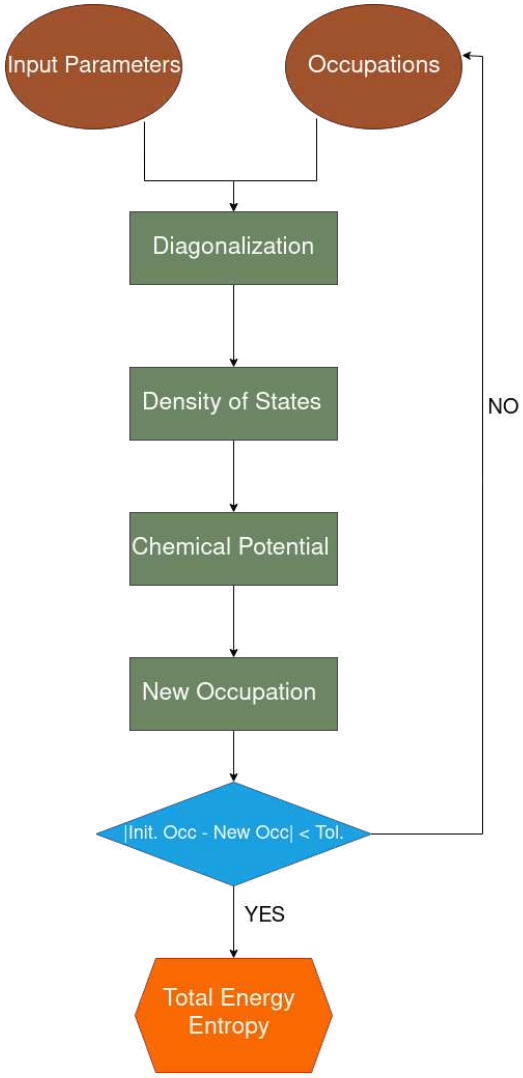

Figure 20 – Schematic representation of self-consistent calculation. In brown are the program inputs, where the initial inputs are U, t and n_e, and the electron occupancies by sites. In green are the steps to be followed to obtain the new occupancies. The blue lozenge checks the convergence of the occupancies, and if they converge, the final step of the calculation is done in the orange box, where the Total Energy and Entropy are obtained.

calculations. The Figure 22 shows schematically how the chemical potential is calculated in both systems studied.

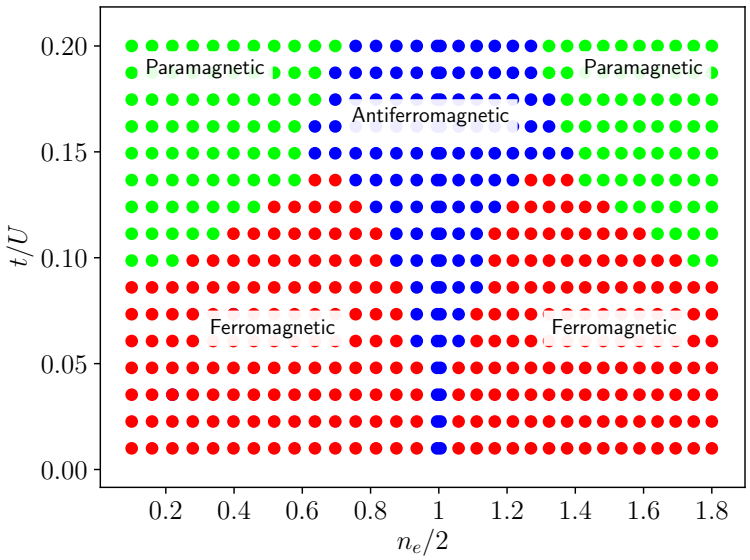

Figure 21 – Magnetic phase diagram obtained by varying the interaction (U) and the doping of the system (n_e). There are three magnetic phases: Ferromagnetism (red dot), Antiferromagnetism (blue dot) and Paramagnetism (green dot). For half filling ($n_e/2$), the system is antiferromagnetic regardless of the value of U.

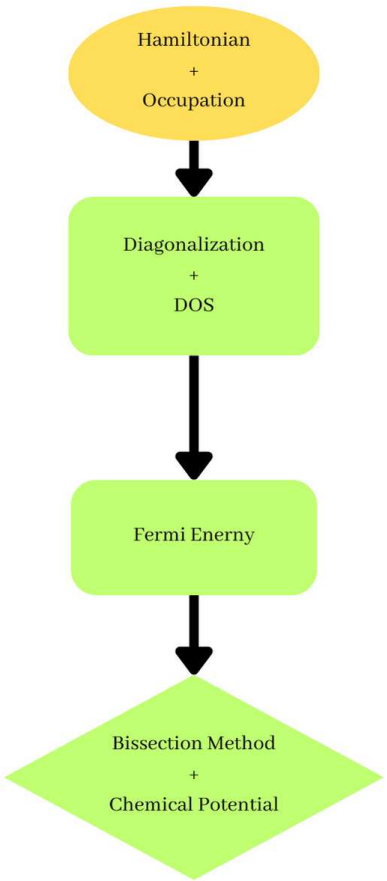

Figure 22 – Diagram of the chemical potential calculation (μ). The yellow frame represents the code's inputs: the system's doping and the tight-binding Hamiltonian. In the green rectangular boxes, the diagonalization of the Hamiltonian and the density of states are calculated, and from these the Fermi energy (E_F), responsible for the first approximation of μ, is estimated. On the green diamond and starting from E_F we use the bisection method and check μ at the ends of the interval until a tolerance of 10^{-7} is reached. The final chemical potential is the average of μ at the ends of the bisection interval after convergence.

B.2 Hartree-Fock code

In this section, we provide the self-consistent code written in FORTRAN90, link: <https://github.com/HGMendonca/Hartree-Fock---Square-lattice>

APPENDIX C – DFT calculation for porphyrin in graphene

In the last 20 years the DFT method has become more relevant in the study of solids (VERMA; TRUHLAR, 2020), in particular in the area of band structure, phonon calculation, charge distribution, among others. In order to understand the physical effects of a porphyrin-like molecule embedded in graphene, we performed a DFT calculation for the structure shown in Fig. 23, using the open-source Quantum Espresso software (GIANNOZZI et al., 2009; GIANNOZZI et al., 2017). Using the software, we converged on the atomic positions with the lowest potential energy, found the symmetry of the solid, calculated the wave functions for all the electrons, and calculated the band structure of the material. We used the pseudopotentials Fe.pbe-spn-kjpaw_psl.1.0.0.UPF, N.pbe-n-kjpaw_psl.1.0.0.UPF and C.pbe-n-kjpaw_psl.1.0.0.UPF from the Quantum Espresso pseudopotential database: <http://www.quantum-espresso.org/pseudopotentials>

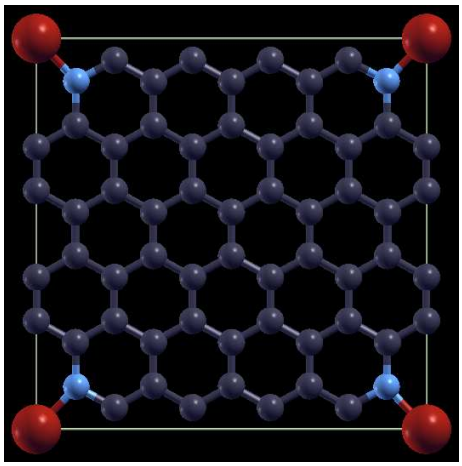

Figure 23 – Porphyrin-like molecular structure embedded in graphene with orthorhombic D_{4h} symmetry. Iron atom, Nitrogen atom and Carbon atom in red, blue and purple respectively.

Once we had all the DFT results from Quantum Espresso, we wannierized the system using the open-source software Wannier90 (MOSTOFI et al., 2014), which reproduced the DFT bands using the Wannier basis, Fig. 24, projecting the $d_{xy}; d_{xz}; d_{yz}; d_{z^2}, d_{x^2-y^2}$ atomic orbitals onto the Iron atom, the $s; p_x; p_y; p_z$ orbitals onto the Nitrogen atoms, and the same representation for the graphene unit cell onto the Carbon atoms, Fig. 6.

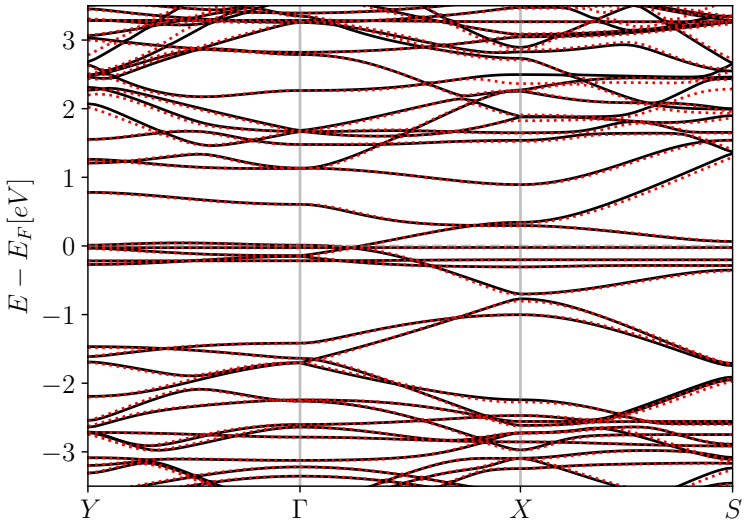

Figure 24 – DFT (black curves) and Wannier (red curves) band structure for porphyrin-like embedded in graphene. Near the Fermi level, the flat curves indicate the location of the d-type orbitals of the iron atom.

From the results of the wannierization, we obtain the hoppings of the TB Hamiltonian in the Wannier basis.

A posteriori, we will include correlation effects via the Density Matrix Renormalization Group (DMRG) (WHITE, 1992; BÜSSER; MARTINS; FEIGUIN, 2013), but for this, the tight-binding orbitals need to be based on the atomic basis and not the Wannier basis. We hope that in the future, with the help of the PAOFLOW (Buongiorno Nardelli et al., 2018; CERASOLI et al., 2021) software, we will be able to converge the orbitals in the desired basis from the DFT data.

All the input files are available at the link: <https://github.com/HGMendonca/DFT-Wannier90>.

APPENDIX D – RPA code

In this appendix we will present the codes developed in each stage of the RPA calculation, in each Section we will present the modules and a summary of what each of them have done. For all the codes presented, the case that will be shown is for doping $n = 4.35$. All the codes are available at the link: <https://github.com/HGMendonca/LaCrAsO---MRPA-Method>.

It is necessary to make it clear that in all the codes where "CALL CHEMPOT" is used, the value of μ is taken for doping $n = 4.35$, which is why we did not put this code in this dissertation; the list of values of μ has already been shown in Table 4.2. It should also be noted that the "input-ws.dat" file stores the hopping parameters provided by (WANG et al., 2017). All the "interface" modules define the invariable parameters in all the codes and also define the global variables of the codes.

D.1 Electronic structure

To calculate the band structure, a FORTRAN90 code was created with a module ('interface'), a subroutine ('TIGHTB(BKX,BKY)') and a main program ('PATH'), and the code will be presented in that order. All the codes are available at the link: <https://github.com/HGMendonca/LaCrAsO---MRPA-Method/tree/main/Band-structure>.

D.2 Fermi surface

Calculating the Fermi surface requires a module ("interface"), three subroutines ("chempot", "tight" and "alphabeta") and a main programme ("band"). The codes are available at the link: <https://github.com/HGMendonca/LaCrAsO---MRPA-Method/tree/main/FS>.

D.3 Calculation of χ_0

We calculated χ_0 in the entire Brillouin zone, using the "interface" module and the "chempot" and "tight" subroutines, as well as the main "SUSPOL" code. The codes are available at the link: <https://github.com/HGMendonca/LaCrAsO---MRPA-Method/tree/main/Non-interacting>.

D.4 Calculation of χ_S and χ_C

To calculate the interacting susceptibilities, we needed a module ("interface"), a main code ("rpasus"), and four subroutines, two of which are "chempot" and "tight". The codes

are available at the link: <https://github.com/HGMendonca/LaCrAsO---MRPA-Method/tree/main/Interacting>.

D.5 Calculation of Γ and the eigenvalues and eigenvectors

The last step refers to the Γ calculus and its diagonalisation. To do this, we use a module ("interface"), five subroutines ("susbicub", "bcuint", "bcucof", "eigenvalue" and "diagonal"), and a main code ("eigensg"). The codes are available at the link: <https://github.com/HGMendonca/LaCrAsO---MRPA-Method/tree/main/Gamma>.